

Advanced Capabilities of the PYXAID Program: Integration Schemes, Decoherence Effects, Multiexcitonic States, and Field-Matter Interaction

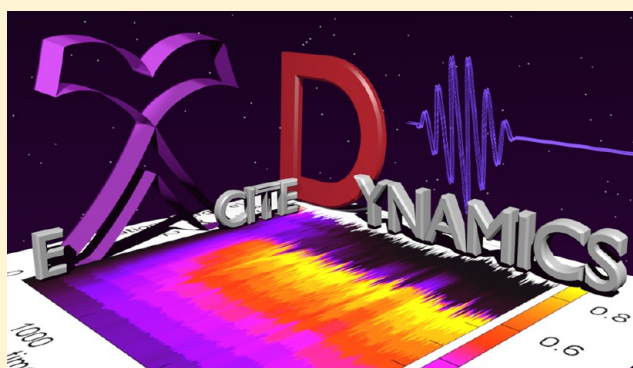
Alexey V. Akimov^{†,‡} and Oleg V. Prezhdo^{*,†}

[†]Department of Chemistry, University of Rochester, Rochester, New York 14627

[‡]Chemistry Department, Brookhaven National Laboratory, Upton, New York, 11973

S Supporting Information

ABSTRACT: In our previous work [*J. Chem. Theory Comput.* 2013, 9, 4959], we introduced the PYXAID program, developed for the purpose of performing nonadiabatic molecular dynamics simulations in large-scale condensed matter systems. The methodological aspects and the basic capabilities of the program have been extensively discussed. In the present work, we perform a thorough investigation of advanced capabilities of the program, namely, the advanced integration techniques for the time-dependent Schrodinger equation (TD-SE), the decoherence corrections via decoherence-induced surface hopping, the use of multiexciton basis configurations, and the direct simulation of photoexcitation via explicit light–matter interaction. We demonstrate the importance of the mentioned features by studying the electronic dynamics in a variety of systems. In particular, we demonstrate that the advanced integration techniques for solving TD-SE may lead to a significant speedup of the calculations and provide more stable solutions. We show that decoherence is necessary for accurate description of slow relaxation processes such as electron–hole recombination in solid C₆₀. By using multiexciton configurations and direct, nonperturbative treatment of field–matter interactions, we found nontrivial optimality conditions for the multiple exciton generation in a small silicon cluster.



1. INTRODUCTION

The dynamics of excited states has been a subject of multiple studies for many years.^{1,2} Such great interest is associated with the vital role of charge transport and energy relaxation in essentially all molecular and solid state systems, spanning a wide range of objects, from biological systems to diverse synthetic materials. Biological examples include light-harvesting antennas in photosynthetic complexes,^{3–7} retinal chromophores in eye receptors,^{8–10} and nucleotide base pairs in DNA.^{11–13} Man-made materials are exemplified by organic molecular dyes^{14–18} and crystals,^{19–23} inorganic quantum dots^{24–29} and crystals,^{30–35} and a variety of hybrid structures^{36–39} that all can be used for photovoltaic and photocatalytic applications.^{2,40–42} The interest in the dynamics of the electronic degrees of freedom and its enormous practical implications drives the demand for accurate, efficient, and convenient tools for modeling of charge transfer and energy relaxation processes.

A number of programs capable of performing such a task have been reported, including Newton-X,^{43,44} MOLPRO,^{45,46} MNDO,^{47,48} CPMD,^{49,50} and Octopus,^{51–53} each with its own advantages and limitations. In our recent work,⁵⁴ we have presented the PYXAID program (Python EXtension for Ab Initio Dynamics) for nonadiabatic molecular dynamics (NAMD). We extensively discussed the general workflow and basic

capabilities of the PYXAID program, along with the related theoretical background. In the present work, we demonstrate the advanced capabilities of the program and the benchmark calculations to showcase the role and importance of a proper simulation setup, including utilization of different algorithms for integrating the time-dependent Schrodinger equation (TD-SE), incorporation of decoherence corrections, explicit treatment of the field–matter interaction, and the use of multiple exciton basis states. We demonstrate these methodologies by application to important problems, studied recently by experimentalists.

The paper is organized as follows. In section 2, we discuss the importance of each methodological aspect that constitutes the advanced capabilities of the PYXAID package. We provide a detailed formulation of the corresponding methodologies. Namely, subsection 2.1 presents the integration algorithms for the TD-SE; subsection 2.2 describes the decoherence corrections via the decoherence induced surface hopping (DISH) algorithm;⁵⁵ subsection 2.3 discusses the explicit treatment of the field–matter interaction in electronic nonadiabatic dynamics.

In section 3, we present the results of our simulations of the electronic dynamics in a number of systems. Subsection 3.1

Received: October 25, 2013

Published: January 10, 2014

discusses the roles of integrators and basis size in solving the TD-SE, as applied to hot electron relaxation in solid pentacene. Subsection 3.2 highlights the role of decoherence effects, as exemplified by slow nonexponential relaxation dynamics of the lowest energy excitons in solid fullerene. In subsection 3.3, we study various ways of multiple exciton generation in a small silicon cluster. This example demonstrates both the explicit field-matter interaction and the use of multiple exciton (singly and doubly excited) basis states. Section 4 concludes the work by summarizing the most important findings—both from the theoretical point of view and from the perspective of materials and applications.

2. THEORETICAL METHODOLOGY

2.1. Integration Schemes for the TD-SE. An accurate and fast solution of the TD-SE

$$\frac{d}{dt}\vec{c}(t) = H(t)\vec{c}(t) \quad (1)$$

is one of the key requirements for any trajectory surface hopping (TSH) algorithm, such as the fewest switches surface hopping (FSSH) method, developed by Tully.⁵⁶ In eq 1, $\vec{c}(t) = (c_0(t) \ c_1(t) \ \dots \ c_n(t))^T$ is a time-dependent vector of amplitudes of adiabatic states in the expansion of the wave function describing the system of interest, $H(t)$ is an $n \times n$ electronic Hamiltonian matrix, which may be explicitly time-dependent. Most often, $H(t)$ is dependent on time parametrically, through the dependence on evolving nuclear coordinates. As a consequence, there are two integration time steps, dt_{el} and dt_{nuc} , corresponding to the fast electronic and slow nuclear time scales. In the classical path approximation (CPA), dt_{nuc} is used to precompute a molecular dynamics trajectory. It is also convenient to abbreviate all quantities in terms of the two time scales—nuclear time t_{nuc} , defined as the time offset between the current time and the start of the whole simulation, and the electronic time t_{el} , defined as the time offset between the current time and the last nuclear time step. The number of electronic time steps per one nuclear step is $n_{\text{el}} = (dt_{\text{nuc}})/(dt_{\text{el}})$.

The second-order finite difference method (Euler scheme) with interpolation of the Hamiltonian is the simplest possible algorithm for solving the TD-SE, eq 1. It is defined by

$$H_{\text{int}}(t_{\text{nuc}}; t_{\text{el}}) = H(t_{\text{nuc}}) + \frac{H(t_{\text{nuc}} + dt_{\text{nuc}}) - H(t_{\text{nuc}})}{dt_{\text{nuc}}} t_{\text{el}} \quad (2a)$$

$$\vec{c}(t_{\text{nuc}}; t_{\text{el}} + dt_{\text{el}}) = \vec{c}(t_{\text{nuc}}; t_{\text{el}} - dt_{\text{el}}) - \frac{2 \cdot i \cdot dt_{\text{el}}}{\hbar} H_{\text{int}}(t_{\text{nuc}}; t_{\text{el}}) \vec{c}(t) \quad (2b)$$

$$\vec{c}(0; dt_{\text{el}}) = \vec{c}(0; 0) - \frac{i \cdot dt_{\text{el}}}{\hbar} H_{\text{int}}(0; 0) \vec{c}(0, 0) \quad (2c)$$

The integration steps above include the Hamiltonian interpolation step (eq 2a) and the propagation of the coefficients \vec{c} (eqs 2b and 2c). This algorithm is invoked by setting the params[“namd_algo”] parameter to 11.

A slight modification of the algorithm described by eq 2 is obtained by using the symmetric difference to approximate the slope of the Hamiltonian:

$$H_{\text{int}}(t_{\text{nuc}}; t_{\text{el}}) = H(t_{\text{nuc}}) + \frac{H(t_{\text{nuc}} + dt_{\text{nuc}}) - H(t_{\text{nuc}})}{dt_{\text{nuc}}} t_{\text{el}}, \quad t_{\text{nuc}} = 0 \quad (3a)$$

$$H_{\text{int}}(t_{\text{nuc}}; t_{\text{el}}) = H(t_{\text{nuc}}) + \frac{H(t_{\text{nuc}} + dt_{\text{nuc}}) - H(t_{\text{nuc}} - dt_{\text{nuc}})}{2dt_{\text{nuc}}} t_{\text{el}}, \quad t_{\text{nuc}} > 0 \quad (3b)$$

$$\vec{c}(t_{\text{nuc}}; t_{\text{el}} + dt_{\text{el}}) = \vec{c}(t_{\text{nuc}}; t_{\text{el}} - dt_{\text{el}}) - \frac{2 \cdot i \cdot dt_{\text{el}}}{\hbar} H_{\text{int}}(t_{\text{nuc}}; t_{\text{el}}) \vec{c}(t) \quad (3c)$$

$$\vec{c}(0; dt_{\text{el}}) = \vec{c}(0; 0) - \frac{i \cdot dt_{\text{el}}}{\hbar} H_{\text{int}}(0; 0) \vec{c}(0, 0) \quad (3d)$$

This algorithm is invoked by setting the params[“namd_algo”] parameter to 10.

Although the leapfrog schemes, eqs 2 and 3, are sufficiently stable and accurate $O(dt)$, they require small electronic time steps, normally 1–10 attoseconds. Larger integration steps lead to instabilities and divergences and therefore cannot be used for practical calculations. In addition, the norm of the wave function given by the sum of squares of the amplitudes, $\sum_{i=1}^n |c_i|^2$, is not strictly conserved. In the long run, or when a large integration time step is used, this may lead to an unphysical solution, misrepresenting the electronic evolution.

Utilization of non-Markovian TSH methods, such as DISH, provides another reason for having efficient and stable integration schemes. As will be discussed in section 2.2, unlike FSSH–CPA, DISH requires integration of eq 1 for each stochastic realization of the surface hopping trajectory. Because the typical number of such stochastic realizations needed for statistically converged results varies from 100 to many thousands, the integration of the TD-SE may become the bottleneck of the calculations. Keeping in mind that FSSH or DISH may be combined with on-the-fly electronic structure calculations, one may see that the algorithms allowing utilization of large integration time steps are highly desirable.

Among the options for such integrators is the one based on analytic integration of eq 1. Assuming that the Hamiltonian matrix is slowly varying on the time scale of the nuclear integration time step, one can use its average value over such an interval (or the value at the midpoint) to integrate eq 1 exactly:

$$\vec{c}(t_{\text{nuc}}; t_{\text{el}}) = \exp\left(-\frac{i \cdot t_{\text{el}}}{\hbar} \tilde{H}(t_{\text{nuc}})\right) \vec{c}(t_{\text{nuc}}; 0) \quad (4)$$

where the Hamiltonian $\tilde{H}(t) = \tilde{H}(t_{\text{nuc}})$ is constant at each time interval $t \in (t_{\text{nuc}}; t_{\text{nuc}} + t_{\text{el}}]$.

To evaluate the matrix exponent in eq 4, the Hamiltonian is diagonalized by solving the eigenvalue problem:

$$\tilde{H}\vec{u} = \vec{u}\vec{E} \Rightarrow \tilde{H} = \vec{u}\vec{E}\vec{u}^+ \quad (5)$$

where \vec{E} is the diagonal matrix of eigenvalues and \vec{u} is the matrix of eigenvectors. This can be done in an efficient manner, because the Hamiltonian is Hermitian. Using the orthonormality of the eigenvectors, $\vec{u}\vec{u}^+ = \vec{u}^+\vec{u} = I$, and the Taylor series representation of the exponential function, one can compute

$$\begin{aligned}\exp(\tilde{H}) &\equiv I + \tilde{H} + \frac{\tilde{H}^2}{2!} + \dots \\ &= \tilde{u}\tilde{L}\tilde{u}^+ + \tilde{u}\tilde{E}\tilde{u}^+ + \frac{1}{2!}\tilde{u}\tilde{E}^2\tilde{u}^+ + \dots \\ &= \tilde{u} \exp(\tilde{E}) \tilde{u}^+\end{aligned}\quad (6)$$

The matrix \tilde{E} is diagonal, and therefore, its exponential, $\exp(\tilde{E})$, can be easily evaluated as $(\exp(\tilde{E}))_{ij} = \exp(\tilde{E}_{ij})$. This algorithm is invoked by setting the params["namd_algo"] parameter to 2. As it follows from eq 4, the evolution of the electronic coefficients $\tilde{c}(t)$ based on such an integration scheme is time-reversible and norm-conserving. This means that the electronic integration time step, dt_{el} , may be increased up to the value of the nuclear integration time step, dt_{nuc} .

For large basis sizes, the performance of the above method may decrease due to the necessity of matrix diagonalization at every nuclear time step. To alleviate this problem, we developed the TD-SE solution scheme based on the Liouville formalism followed by the Trotter factorization^{57,58} of the evolution operator. The equations of motion, eq 1, correspond to the Liouville operator:

$$\begin{aligned}iL &= \sum_{i=0}^{N-1} \dot{c}_i \frac{\partial}{\partial c_i} \\ &= \sum_{i=0}^{N-1} \sum_{j=0}^{N-1} \left(-\frac{i}{\hbar} H_{ij} \right) c_j \frac{\partial}{\partial c_i} \\ &= \sum_{i=0}^{N-1} \left(-\frac{i}{\hbar} H_{ii} \right) c_i \frac{\partial}{\partial c_i} + \sum_{i=0}^{N-1} \sum_{j>i}^{N-1} \\ &\quad -\frac{i}{\hbar} \left(H_{ij} c_j \frac{\partial}{\partial c_i} + H_{ji} c_i \frac{\partial}{\partial c_j} \right) \\ &= \sum_{i=0}^{N-1} iL_i^{(1)} + \sum_{i=0}^{N-1} \sum_{j>i}^{N-1} iL_{ij}^{(2)}\end{aligned}\quad (7)$$

which can be factorized in a symmetric way:

$$\begin{aligned}\exp(iL \cdot dt_{\text{el}}) &= \exp\left(\sum_{i=0}^{N-1} iL_i^{(1)} \cdot \frac{dt_{\text{el}}}{2}\right) \exp\left(iL_{01}^{(2)} \cdot \frac{dt_{\text{el}}}{2}\right) \\ &\quad \exp\left(iL_{02}^{(2)} \cdot \frac{dt_{\text{el}}}{2}\right) \dots \exp\left(iL_{0(N-1)}^{(2)} \cdot \frac{dt_{\text{el}}}{2}\right) \exp\left(iL_{12}^{(2)} \cdot \frac{dt_{\text{el}}}{2}\right) \\ &\quad \dots \exp\left(iL_{1(N-1)}^{(2)} \cdot \frac{dt_{\text{el}}}{2}\right) \dots \exp\left(iL_{(N-2)(N-1)}^{(2)} \cdot \frac{dt_{\text{el}}}{2}\right) \\ &\quad \exp\left(iL_{(N-2)(N-1)}^{(2)} \cdot \frac{dt_{\text{el}}}{2}\right) \dots \exp\left(iL_{1(N-1)}^{(2)} \cdot \frac{dt_{\text{el}}}{2}\right) \dots \exp\left(iL_{12}^{(2)} \cdot \frac{dt_{\text{el}}}{2}\right) \\ &\quad \cdot \frac{dt_{\text{el}}}{2} \exp\left(iL_{0(N-1)}^{(2)} \cdot \frac{dt_{\text{el}}}{2}\right) \dots \exp\left(iL_{02}^{(2)} \cdot \frac{dt_{\text{el}}}{2}\right) \\ &\quad \exp\left(iL_{01}^{(2)} \cdot \frac{dt_{\text{el}}}{2}\right) \exp\left(\sum_{i=0}^{N-1} iL_i^{(1)} \cdot \frac{dt_{\text{el}}}{2}\right)\end{aligned}\quad (8)$$

The action of the operators $\exp(iL_i^{(1)} dt)$ and $\exp(iL_{ij}^{(2)} dt)$ is given by (see detailed derivation in section A of the Supporting Information):

$$\begin{aligned}\exp(iL_i^{(1)} dt) &= \exp\left(\alpha_i \cdot dt \cdot c_i \frac{\partial}{\partial c_i}\right): c_i \rightarrow \exp(\alpha_i \cdot dt) c_i \\ &= \left[\cos\left(\frac{dt}{\hbar} \varepsilon_i\right) - i \sin\left(\frac{dt}{\hbar} \varepsilon_i\right) \right] c_i\end{aligned}\quad (9a)$$

$$\begin{aligned}\exp(iL_{ij}^{(2)} dt) &= \exp\left(dt \cdot \beta_{ij} \left(c_j \frac{\partial}{\partial c_i} - c_i \frac{\partial}{\partial c_j} \right) \right): \begin{pmatrix} c_i \\ c_j \end{pmatrix} \\ &\rightarrow \begin{pmatrix} \cos(dt \cdot \beta_{ij}) & \sin(dt \cdot \beta_{ij}) \\ -\sin(dt \cdot \beta_{ij}) & \cos(dt \cdot \beta_{ij}) \end{pmatrix} \begin{pmatrix} c_i \\ c_j \end{pmatrix}\end{aligned}\quad (9b)$$

$$\alpha_i = -\frac{i}{\hbar} H_{ii} = -\frac{i}{\hbar} E_i \quad (9c)$$

$$\beta_{ij} = -\frac{i}{\hbar} H_{ij} = -d_{ij} \quad (9d)$$

The last equalities in eqs 9c and 9d are specifics for the Hamiltonian expressed in an adiabatic basis. The quantities E_i and d_{ij} are the energies of the adiabatic states and the nonadiabatic couplings (NAC), respectively. We refer the reader to our earlier work for a more detailed discussion of these quantities.⁵⁴

As seen from eq 9, the operators of the first type, $\exp(iL_i^{(1)} dt)$, simply propagate the phase of each electronic state, while the operators of the second type, $\exp(iL_{ij}^{(2)} dt)$, describe population transfer between each pair of electronic state. Each of these operators is unitary, and, thus, their action conserves the sum of the norms of the amplitudes they act on. As a result, the norm of the wave function is also conserved exactly. Similarly to the analytic solution presented above, the form of eq 9 allows one to use sufficiently large electronic time steps. The symmetric splitting scheme, eq 8, makes the propagator time-reversible, which is a desired property of integrators because it complies with the symmetry of the space–time continuum. The main advantage of this algorithm in comparison to the one based on the analytic solution, eq 4, is that no matrix diagonalization is required. All operations are explicit and numerically efficient, allowing a large number of basis states to be used. The algorithm described above is invoked by setting the params["namd_algo"] parameter to 0.

2.2. Loss of Coherence in the Electronic Subsystem—Decoherence Induced Surface Hopping. The approximations leading to the TSH methods reduce the exact TD-SE for the joint electronic–nuclear wave function to the TD-SE for the electronic amplitudes only, eq 1, joint with classical equations of motion for nuclear degrees of freedom.² The reduction transforms a nuclear wavepacket into a classical phase-space point. Nuclear wave functions are no longer available, even though they enter expressions for transitions rates, for instance, the Franck–Condon factor in Fermi's golden rule. In a fully quantum treatment, the evolution of the electronic subsystem is obtained by integrating out the nuclear degrees of freedom. The integration over the diverging nuclear wavepackets (Figure 1) causes a loss of coherence in the electronic subsystem: A superposition of several electronic states becomes a statistical mixture. Decoherence causes the electronic wave function to collapse to adiabatic states. Equivalently, decoherence makes the off-diagonal elements of the electronic density matrix decay to zero. The quantum Zeno effect^{59–63} illustrates the strong influence of decoherence on quantum transitions. By treating

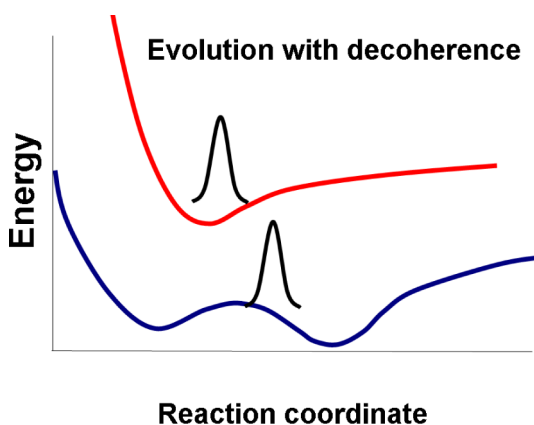


Figure 1. Divergence of nuclear wavepackets associated with different electronic states causes loss of coherence within the electronic subsystem. This effect is missing if nuclear motion is treated classically, as in the FSSH. It can be introduced in semiclassical approaches, such as DISH.

nuclear motions classically, the FSSH approach excludes decoherence effects.

The decoherence time is given by the time-scale of divergence of the nuclear wavepackets (Figure 1). It is related directly to the phonon-induced pure-dephasing time that appears in the optical response theory.^{64–67} The inverse of the pure-dephasing time determines single-particle (homogeneous) spectral linewidths, and therefore, it is accessible experimentally. The pure-dephasing time can be computed within the scope of the optical response theory, from the autocorrelation function of the electronic energy gap fluctuating along the MD trajectory due to nuclear motions. Alternatively, the decoherence time can be obtained from the wavepacket description (Figure 1), assuming, for instance, that each nuclear degree of freedom is a Gaussian wavepacket with the width given by the thermal de Broglie wavelength.^{68–71}

Decoherence effects should be included in the NA-MD simulation, if the decoherence time is shorter than the time of coherent electronic transition. For instance, decoherence can be ignored during the rapid relaxation along the quasi-continuous manifold of excited electronic states in nanoscale systems. Such a relaxation process can be modeled successfully by the quantum-classical FSSH scheme.^{24,72} In contrast, decoherence effects are very important for slow electron–hole recombination across the band gap.^{25,73} A straightforward quantum-classical treatment overestimates the recombination rate by several orders of magnitude.

The nature of the electronic states manifold over which electronic transitions of interest take place provides an indication for the need of a decoherence correction. Well separated energy levels and localized states suggest that decoherence effects should be taken into account. This situation is very common for molecules, quantum-confined systems (e.g., quantum dots, nanotubes), and some condensed matter materials. On the contrary, materials with wide, dispersed electronic band structure, such as metals and most of the solid state semiconductors, can be well described by the fully coherent FSSH or even with the mean-field techniques. A high density of states in such systems will facilitate fast intrinsic electronic transitions, and decoherence effects will play no practical role.

Decoherence induces stochastic collapse of the wave function to adiabatic states. According to the standard rules of quantum mechanics, the probability to collapse to the eigenstate i is

determined by the square of the coefficient in the expansion of the TD wave function in the eigenstate basis, $|c_i|^2$. In this interpretation, decoherence is qualitatively similar to surface hopping,⁷⁴ leading to the DISH scheme.⁵⁵ A wide variety of methods to include decoherence effects into quantum-classical NA-MD simulations have been proposed.^{66,69–71,75–81} Most methods introduce decoherence as a correction to the surface hopping scheme. By interpreting decoherence in the stochastic way, DISH realizes a surface hopping algorithm that uses standard probabilistic interpretation of quantum mechanics and obviates the need for additional, *ad hoc* prescriptions for surface hopping probabilities. The PYXAID program implements the DISH algorithm⁵⁵ and adapts it to the CPA implementation of the NA-MD.

Surface hops happen in the DISH method as a result of decoherence in the electronic subsystem. When the semiclassical nuclear wavepacket associated with a given electronic state i moves sufficiently far away from the wavepackets correlated with the other states (Figure 1), the system must decide whether to hop to state i or to remain in the superposition of the remaining states. The DISH algorithm can be summarized in the following sequence of steps:

(1) Propagate all states coherently by solving the TD-SE, eq 13, until a decoherence event takes place. State i decoheres from all other states, when the following condition is met:

$$t_i(t) > \tau_i(t) \quad (10a)$$

Here, t is the physical time, set equal to 0 at the beginning of the NA-MD simulation, t_i is the time since the last decoherence event for state i , and $\tau_i(t)$ is the decoherence time for state i , defined as

$$\frac{1}{\tau_i(t)} = \sum_{j=1, j \neq i}^{N_b} |c_j(t)|^2 r_{ij} \quad (10b)$$

where r_{ij} are the decoherence rates between pairs of electronic states. Note that the decoherence time of eq 10b is time-dependent, because of the time-dependence of the amplitudes $c_i(t)$. Therefore, the quantum dynamics in DISH depends on history and is non-Markovian.

(2) At the decoherence event, either the wave function collapses onto the decohered state i with the probability defined by the state amplitude, $|c_i(t)|^2$, or the decohered state is projected out by setting $c_i(t) = 0$ and renormalizing the resulting wave function, represented by the set of coefficients $\{c_j(t)\}$, $j \neq i$. The time t_i in eq 10a, is reset to 0.

(3) The trajectory must hop to a new state in two situations. (a) If the wave function collapses to state i , and state i is different from the state associated with the nuclear trajectory, the trajectory hops to state i . (b) If state i is projected out while the nuclear trajectory was associated with this state, the trajectory hops to a state $j \neq i$, with the probability given by $|c_j(t)|^2$.

(4) In the original DISH scheme,⁵⁵ the velocity is rescaled after the hop, as in the FSSH. If the rescaling cannot be achieved, the hop is rejected. Decoherence still occurs; however, the wave function is projected on the subspace complementary to that described in step 3. Under the CPA, to maintain the detailed balance, the probability of the hops upward in energy are scaled by the Boltzmann factor:

$$\exp\left(-\frac{E_i - E_j}{k_B T}\right), E_i - E_j > 0 \quad (10c)$$

In the present implementation, the decoherence rates r_{ij} entering eq 10b are precomputed before the NA-MD simulation are started, using the optical response theory.⁸² We choose the optical response formalism among many other methods of computing the decoherence rates, because it requires no adjustable parameters, provides robust results, and can be tested experimentally by comparison with pure-dephasing times and homogeneous optical linewidths. Further, the optical response formalism fits well with the CPA: the dephasing rates are obtained along the CPA trajectory that is used later to carry out the NA-MD.

The transition probabilities in the FSSH-CPA scheme depend on the solution of the TD-SE, eq 1, while the latter is driven by the classical path and is independent of the hopping events. Consequently, the TD-SE is solved only once in the FSSH-CPA. This is not the case with the DISH-CPA, in which a wave function collapse affects further TD-SE solution. Therefore, the TD-SE must be solved for every realization of the stochastic process in the DISH-CPA. The CPU time required to solve the TD-SE scales linearly with the number of realizations of the stochastic process in the DISH-CPA, while it is virtually independent of the number of realizations of the stochastic process in the FSSH-CPA. The additional computational expense depends on the number of configurations in the many-particle basis. For instance, solution of the TD-SE constitutes the CPU bottleneck in the simulations of multiple exciton generation and recombination, involving hundreds of thousands of configurations.^{83,84} Studies of charge-phonon relaxation,^{24,25} charge transfer,^{85–87} and electron–hole recombination⁷² require a small number of configurations, and the majority of the CPU time is spent solving the time-independent SE to obtain the adiabatic basis state and NAC. The computational expenses of the FSSH and DISH without the CPA are approximately equivalent.

2.3. Explicit Field–Matter Interaction. Field–matter interaction is a central part of many applications and is a subject of many studies. For example, no reasonable description of the photoinduced voltage in nanoscale materials would be possible without taking such terms into account explicitly.^{88,89} Simulation of direct photoexcitation may be inevitable for rigorous description of the charge carrier dynamics in dye-sensitized solar cell devices.² For example, Labat et al.^{17,18} studied photoinduced electron injection from a dye to a semiconducting substrate by manually adding electrons to the system and examining the charge density distribution. Although such an approach does not account for detailed time evolution of charge distribution, it does not make any assumption on the nature of the initially prepared excited state. With explicit description of the field–matter interaction, one may study hidden details of the photoexcitation dynamics. In particular, such an approach may be crucial for estimation of the power conversion efficiencies of dye-sensitized solar cells, because there is always an opportunity for smaller quantum yields or involvement of a direct charge transfer mechanism.^{90–92}

Finally, among the most promising complex photovoltaic systems are those based on junctions of several materials, each of which can absorb photons of different energy—so-called Z-schemes.^{93–96} The detailed understanding of complex correlated dynamics of the charge carriers produced in each part of such systems will require explicit treatment of the light–matter interaction in each component of the Z-scheme. Thus, the capability of simulating direct photoexcitation or charge transfer is of great importance. Below, we outline the theoretical

methodology implemented in the PYXAID for such a type of calculations.

The classical Hamiltonian of a charged particle in the presence of the electromagnetic field (\vec{E}, \vec{B}) is given by

$$H = \frac{1}{2m}(\vec{p} - q\vec{A}(\vec{r}, t))^2 + q\varphi(\vec{r}, t) \quad (11)$$

where q , m , \vec{p} , and \vec{r} denote the charge, mass, momentum, and position of the particle, respectively. The vector $\vec{A}(\vec{r}, t)$ and scalar $\varphi(\vec{r}, t)$ potentials are related to the electromagnetic field components (\vec{E}, \vec{B}) as

$$\vec{E}(\vec{r}, t) = -\vec{\nabla}\varphi(\vec{r}, t) - \frac{\partial\vec{A}(\vec{r}, t)}{\partial t} \quad (12a)$$

$$\vec{B}(\vec{r}, t) = \vec{\nabla} \times \vec{A}(\vec{r}, t) \quad (12b)$$

The field–matter interaction Hamiltonian is then given by

$$H' = -\frac{q}{m}\vec{A}(\vec{r}, t)\vec{p} \quad (13a)$$

Here, we assumed the Coulomb gauge: $(\vec{\nabla}, \vec{A}(\vec{r}, t)) = 0 \Leftrightarrow \varphi(\vec{r}, t) = 0$. Using the correspondence principle of quantum mechanics, the plane-wave representation of the electronic states and the dipole approximation, eq 13a, can be simplified to a more common form (see details of derivation in section B of the Supporting Information):

$$H'_{ij} = \frac{2e\hbar}{m_e} \sum_{\vec{k}} \vec{A}_{\vec{k}}(t) \vec{\mu}_{ij,\vec{k}} \cos(\omega_{\vec{k}}t) \quad (13b)$$

where

$$\vec{\mu}_{ij,\vec{k}} \approx \vec{\mu}_{ij} \equiv \sum_{\vec{G}} c_{i,\vec{G}}^* c_{j,\vec{G}} \vec{G} \quad (14)$$

is the transition dipole moment for transition between electronic states i and j .

In our implementation, the quantity, eq 14, is precomputed along the MD trajectory, similarly to the NACs. As with the NACs, it only parametrically depends on nuclear coordinates. The files containing the matrices composed of the elements in eq 14 are called `Hprime_`. In the case when only the gamma point is used, the symmetry of the wave function coefficients, $c_i \vec{G} = c_i - \vec{G}^*$, implies that such matrices are purely imaginary. The transition dipole moments (purely real) can be computed using the following relation:

$$M_{ij} \equiv e\langle\psi_i|\vec{r}|\psi_j\rangle = -i\frac{e\hbar^2}{m_e} \frac{\mu_{ij}}{(E_j - E_i)} \quad (15)$$

The final component that completes the definition of the simulation setup with the explicit light–matter interaction is the light (e.g., laser) pulse envelope function $\vec{A}_{\vec{k}}(t)$. In the current version of the program, two types of pulse envelopes (modulation protocols) are implemented, including the step-function protocol:

$$A(t) = \begin{cases} A, & t \in \left[T_m - \frac{T}{2}, T_m + \frac{T}{2}\right] \\ 0, & \text{otherwise} \end{cases} \quad (16a)$$

and the sawtooth protocol:

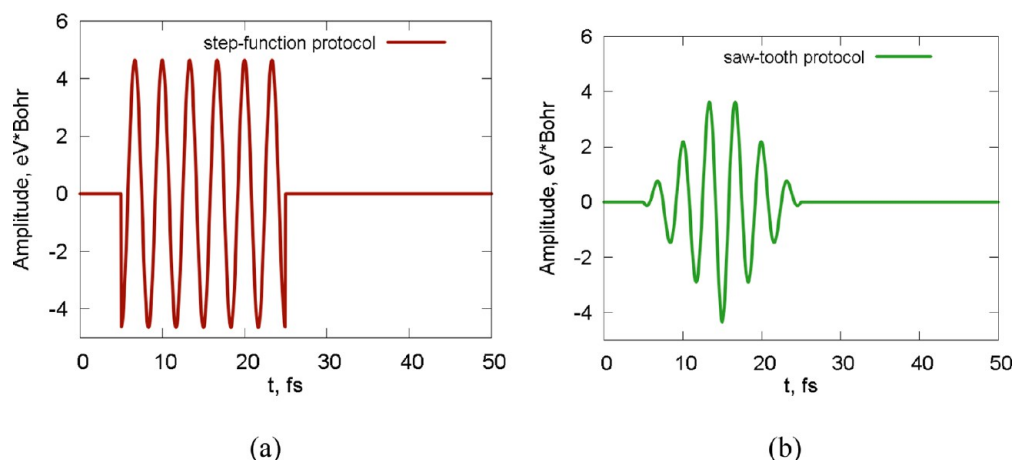


Figure 2. Examples of the envelope protocols: (a) step-function protocol; (b) sawtooth protocol. The parameters used are $T = 20$ fs, $T_m = 15$ fs, $F = 1$ mJ/cm², $\omega = 12\pi/T$ rad/fs.

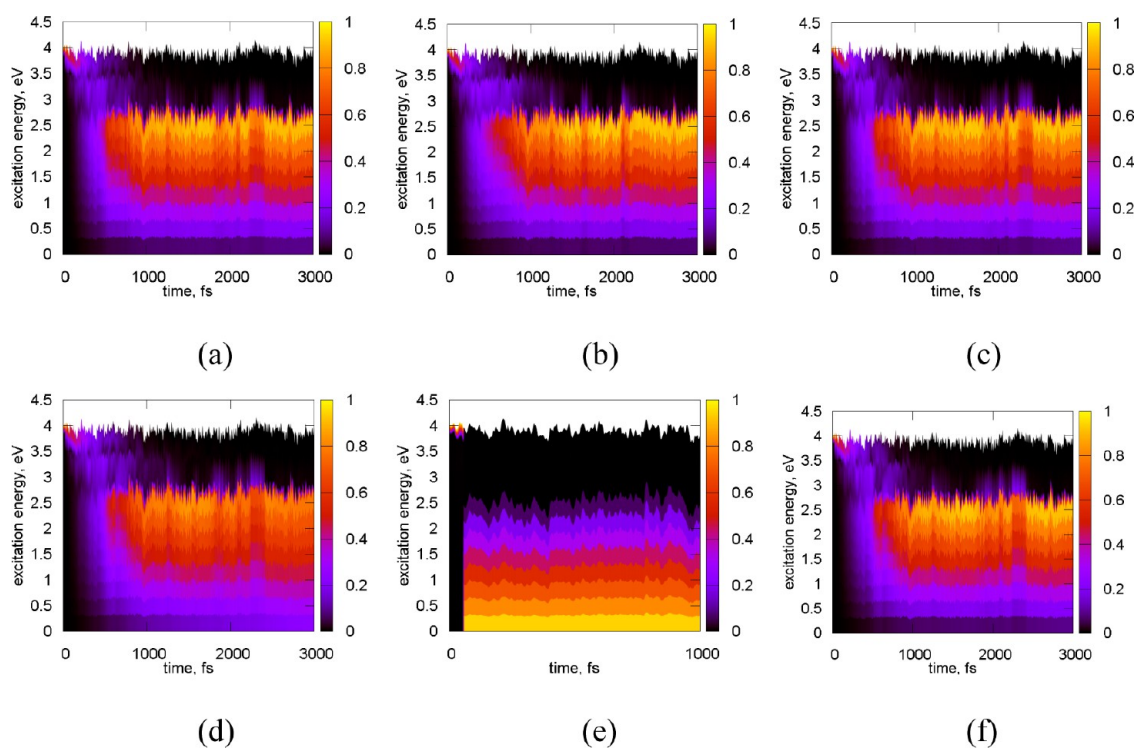


Figure 3. Relaxation dynamics in the crystalline pentacene system with 79 basis states, computed with different methods and integration time steps: (a) integrator 0, $dt = 0.01$ fs; (b) integrator 10 or 11, $dt = 0.01$ fs; (c) integrator 2, $dt = 0.01$ fs; (d) integrator 0, $dt = 1.0$ fs; (e) integrator 10 or 11, $dt = 1.0$ fs; and (f) integrator 2, $dt = 1.0$ fs. Color represents population of a given energy level at a given time.

$$A(t) = \begin{cases} A \frac{t - (T_m - T/2)}{T/2}, & t \in \left[T_m - \frac{T}{2}, T_m \right] \\ A \frac{(T_m + T/2) - t}{T/2}, & t \in \left[T_m, T_m + \frac{T}{2} \right] \\ 0, & \text{otherwise} \end{cases} \quad (16b)$$

The quantities T_m , T , and A are the parameters of the protocols, namely, the center of the pulse in time, the pulse duration, and the maximal amplitude of the envelope function, respectively. The plots of $(e\hbar/m_e)A(t)$ as a function of time are shown in Figure 2 for the two envelope protocols.

The magnitude of parameter A that determines the field strength is related to the experimental parameters, such as

fluence F (measured in J/m²) or intensity I (measured in W/m²). The detailed derivation of such relations and some numerical estimates are given in Supporting Information, section C.

3. RESULTS AND DISCUSSIONS

3.1. Effects of Integrator Scheme, Basis Size, and Integration Time Step. Solution of the TD-SE is one of the central procedures of the NA-MD. It can be performed in a variety of ways. In this section, we benchmark the quality and performance characteristics of the integration schemes (integrators) discussed in section 2.1. The performance of a particular integration scheme is closely related to the basis set size and to the integration time step. The time consumed for solving the TD-SE increases as either the size of the basis set increases or as

the integration time step decreases. It is reasonable to expect that as the integration time step decreases, the accuracy and stability of any integration method increases. One may also expect that larger basis sets may require smaller integration time steps or more advanced methodology for correct description of the dynamics. The purpose of this section is to give quantitative estimates of the relationships outlined above.

To test the four integrators discussed in section 2.1, we compute the relaxation dynamics in crystalline pentacene with the initial excited state prepared ca. 2.0 eV above the CB minimum. For the details of the ground state molecular dynamics sampling, we refer the reader to our previous work,⁵⁴ as we use the same precomputed data as in that study. The results of our calculations employing different integrators and different integration step sizes for the system with the basis set of 79 states are presented in Figure 3.

For a sufficiently small integration time step of 0.01 fs, all integrators are stable and produce identical relaxation dynamics profiles (Figure 3, panels a–c). Both the Trotter splitting method, 0, and the exact method, 2, can employ electronic integration time steps of any sufficiently large magnitude, as large as the nuclear integration time step. This is because these integrators are stable by construction. Our calculations support the above statement, indeed: the TD-SE solution is stable even if a 1 fs electronic integration time step is used, as shown in Figure 3 (panels d and f). At the same time, as it is expected, the finite difference methods, 10 and 11, become unstable for such large time discretization intervals, as manifested in the ultrafast relaxation to the lowest energy level (Figure 3e). The difference in stability of the integrators becomes notable as the integration time step, the basis size, or both get larger. The information about stability is summarized in Table 1 for two additional basis set sizes.

Table 1. Performance and Stability Characteristics of the Tested Integration Schemes under Different Conditions^a

integration time step, fs	integrator 0	integrator 10	integrator 11	integrator 2
7 basis states				
0.01	4.9	4.0	4.0	138.2
0.1	3.9	unstable	unstable	17.1
1.0	3.6	unstable	unstable	4.8
261 basis states				
0.01	1946.1	1874.6	1874.6	n/a
0.1	820.2	unstable	unstable	n/a
1.0	746.7	unstable	unstable	n/a

^aThe performance is measured in ms of wall time per one stochastic realization of 1 ps trajectory per initial condition.

To estimate the performance of the implemented integration schemes for the conditions under which they are stable, we present the wall time required for the corresponding calculations. The scheme based on Trotter factorization (scheme 0) is most robust and efficient. For the smallest integration time-step tested ($dt_{el} = 0.01$ fs), the wall time is practically the same as for the finite-difference methods. As the integration time step gets larger, the methods 0 and 2 remain stable, in contrast to the finite difference methods. At the same time, integration method 2 is significantly slower than method 0. Keeping in mind that the latter gives the accuracy of the exact method even for large integration time steps, it can be considered as the method of choice.

One may find that the acceleration associated with the use of large integration time steps is notably smaller than what is expected from the linear scaling. This is because the reported wall time includes some internal processing procedures, which are slower than the integration itself. Thus, the linear scaling is hidden. The linear scaling is clearly observed when the integration phase of the calculations becomes slower than the other procedures, as is the case for integrator 2 or when larger basis sizes are used.

The efficiency benchmarks presented in Table 1 are obtained for the FSSH method without decoherence. When the decoherence effects are treated with the DISH scheme (as explained in section 2.2), the computational efforts scale with the number of stochastic realizations of the SH algorithm. This means that for each trajectory, the TD-SE needs to be integrated independently, which eventually increases the workload on the integration scheme and makes it crucial to use a robust and efficient scheme. As it is suggested by Table 1, the use of the integrator 0 may have a significant positive impact on productivity of the NA-MD with the DISH.

The effect of the basis set size used in the NA-MD calculation on the details of the relaxation kinetics is illustrated in Figure 4. We consider the relaxation dynamics in pentacene with the fixed integration scheme (params["integrator"] = 0) and time-step (params["dt_elec"] = 0.1 fs). The manifold of the basis configurations consists of the ground state configuration and all possible single excitations from the VB levels to the CB levels in the active space, as shown in Figure 4a. The initial excitation is the same for all three tested basis sizes and corresponds to the HOMO → LUMO+5 transition, also shown in Figure 4a. One can see that a minimalistic basis of seven configurations provides a qualitatively correct description of the relaxation dynamics, although the resolution is relatively poor (Figure 4b). The situation changes with the larger basis set of 79 states (Figure 4c)—one can observe that two intermediate bands are transiently populated, one at 3.5–4 eV and the other at 3–3.5 eV, before the electron relaxes to the LUMO (the excited state with the lowest energy, ~2.5 eV). The addition of a larger number of unoccupied orbitals does not affect the resulting dynamics (Figure 4d), pointing to convergence with respect to the basis set size. Thus, one can conclude that even minimalistic models employing a few states may capture essential dynamics of the relaxation process. The choice of an active space must be physically justified and should include KS orbitals that are expected to participate in a given process.

Generation of a large number of basis configurations may seem a tedious job if done manually. As it has been mentioned before,⁵⁴ one of the key features of our program is a capability to define any complex input structure in a convenient programmatic way, facilitated by the easiness of the Python language used as the main interface language between the program and the user. We have provided the **lazy** module, with the help of which the user can generate all singly and doubly excited configurations between given KS levels. Alternatively, the user can choose to script all necessary basis configurations him- or herself.

3.2. Effect of Decoherence. Relaxation dynamics in many materials may often exhibit non-Markovian properties, most often manifested by nonexponential kinetics. Examples include multiexponential or stretched-exponential dynamics and a commonly encountered initial Gaussian decay. Nonexponential kinetics may be associated with the presence of localized electronic states.^{97–99} Localization may occur in space or energy, with the two often correlated to each other. Decoherence is

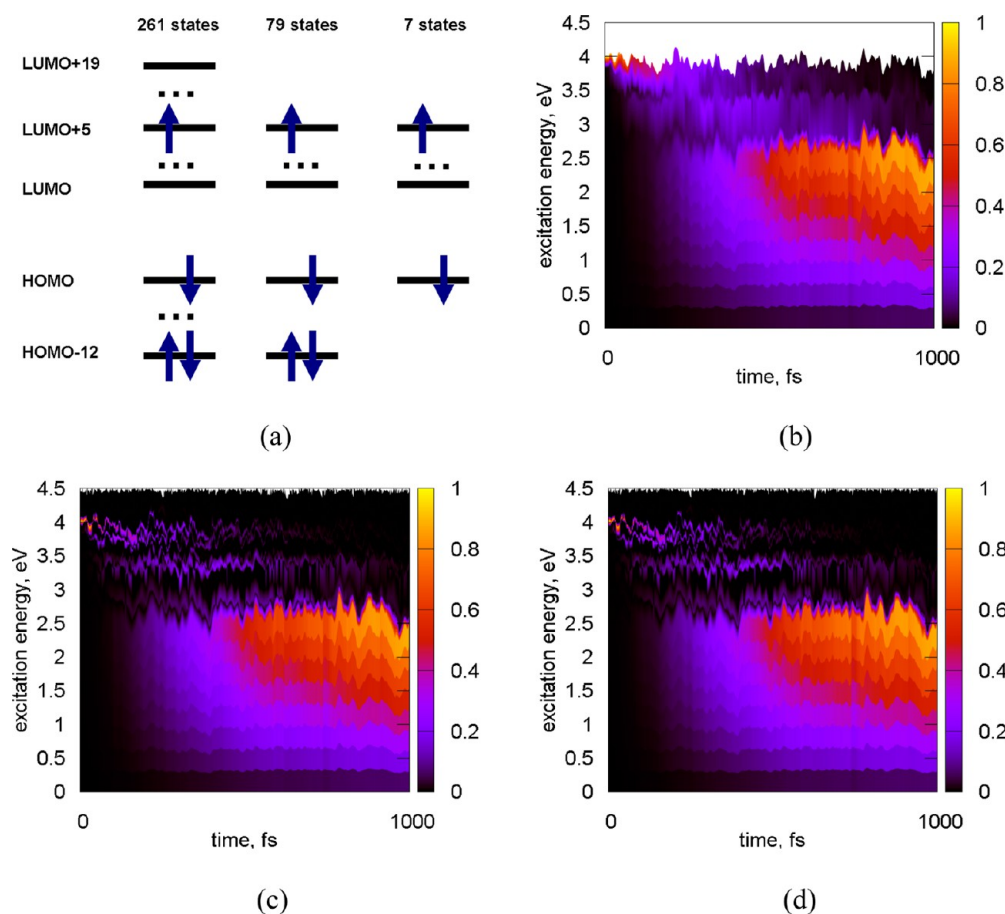


Figure 4. Effect of the basis set size on the electron relaxation dynamics in the pentacene crystal. The manifolds of the excited states (basis configurations) are determined by the active spaces shown in panel a. The integrator 0 is used with the time step $dt = 0.1$ fs. Relaxation dynamics for (b) seven states, (c) 79 states, and (d) 261 states. Color represents population of a given energy level at a given time.

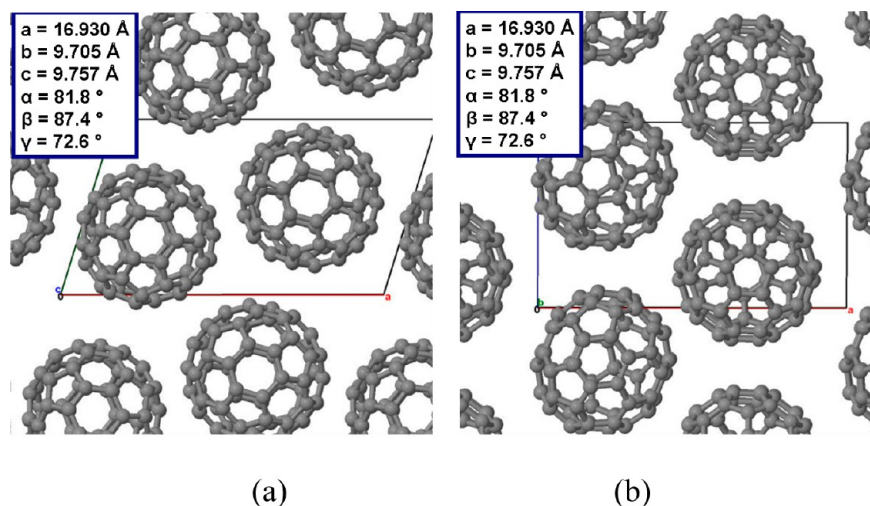


Figure 5. Simulation cell of solid C_{60} : (a) front view; (b) side view.

especially important for localized states: as the difference in the energy and/or probability density of a pair of states increases, the evolution of the nuclear wave functions that correspond to such electronic states becomes more divergent. On the contrary, for closely spaced electronic states (both in energy and in space), coherent dynamics becomes predominant.^{4,6,100,101}

Most of the time, electronic states in solids are delocalized and, therefore, may exhibit coherent dynamics. In such cases, mean-

field theories and the original, fully coherent FSSH procedure are well-grounded.^{102,103} However, solid-state materials may also have strongly localized states, such as those of impurities or defects. Solid C_{60} is remarkable in this respect due to its intrinsic electronic structure that shows the presence of localized states, manifesting crystalline C_{60} as an intrinsically molecular system.^{104–106} The presence of localized states makes the decoherence effects extremely important. In particular, these

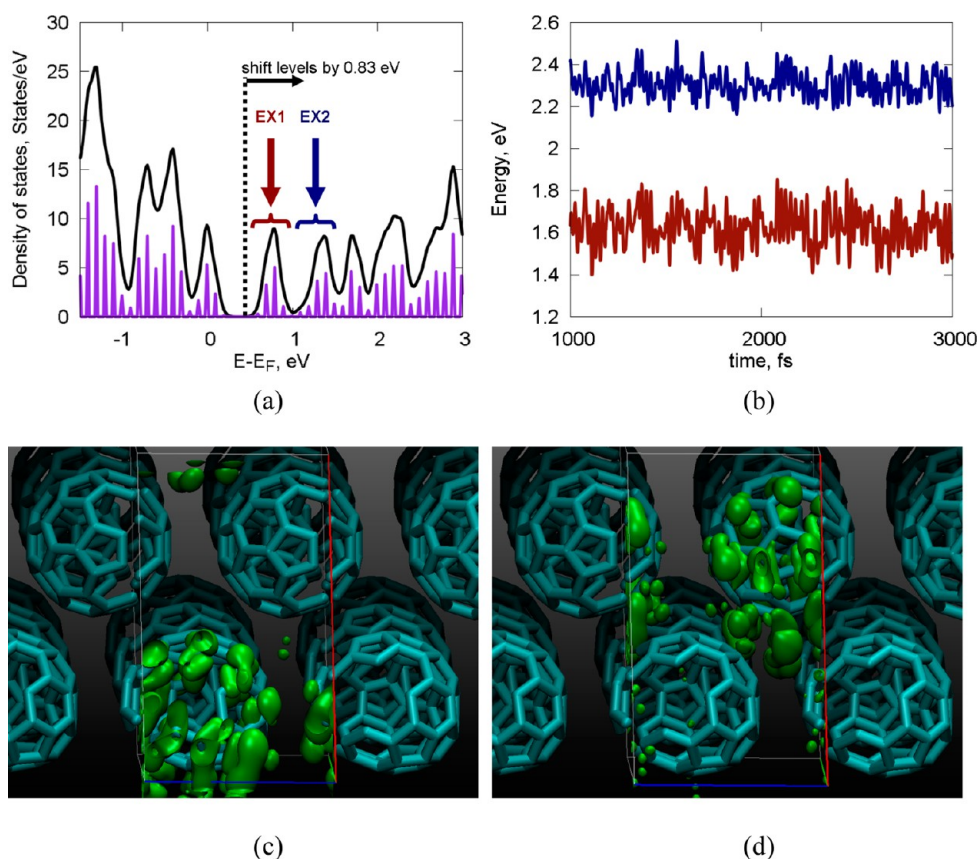


Figure 6. (a) Density of states of crystalline fullerene, computed at the PBE level. The arrows indicate initially excited levels (bands) considered in the NA-MD simulations. (b) The 2 ps evolution of the lowest energy configurations in the first (red) and second (blue) excited state bands. Panels c and d illustrate the localized nature of the two lowest-energy virtual KS orbitals in the LUMO band.

effects are among the major factors leading to the non-Markovian dynamics.^{98,99,107–109}

To demonstrate the importance of decoherence effects and to test our implementation of the DISH scheme⁵⁵ that takes such effects into account, we consider the relaxation of the first excited state of the crystalline C_{60} . Experimentally, this process is known to be relatively slow—the longest component of the multi-exponential fit gives a time scale on the order of 100 ps.¹⁰⁸

The simulation cell used in our calculations contains two C_{60} molecules and is shown in Figure 5. The geometry and unit cell optimization, ground state molecular dynamics, and other electronic structure calculations have been performed using the Quantum Espresso package.¹¹⁰ For all calculations we utilize the PBE functional^{111,112} and the plane-wave representation of the electronic Kohn–Sham orbitals. Core electrons are taken into account with the help of the ultrasoft atomic pseudopotentials.¹¹³ We utilize a converged plane-wave basis with a kinetic energy cutoff of 40 Ry. We sample the first Brillouin zone with the Γ point only, because the zone is small and the occupied states have little dispersion.¹⁰⁵ Ground state molecular dynamics trajectories are sampled from the NVT ensemble using the Verlet¹¹⁴ scheme combined with the Andersen thermostat.¹¹⁵ A 10 ps trajectory is obtained with the integration time step of 1 fs and the Andersen thermostat collision frequency of 25 ps^{−1}.

The experimental value for the HOMO–LUMO gap varies in the range from 1.6 to 2.0 eV.^{116,117} Our value, ca. 0.8 eV, computed at the PBE level (Figure 6a) is notably reduced and can be increased with the help of more accurate electronic structure calculations.¹¹⁸ For the purposes of the nonadiabatic

dynamics simulation, we correct the energies of the virtual orbitals by a rigid shift, to match the experimental band gap. Such a technique is known as the “scissor operator” method and has been used to correct the self-interaction error of pure DFT functionals in many systems.^{119–122}

Although it is often required to adjust energy levels, the methodology based on pure density functionals allows one to perform the computations of relatively long MD trajectories. Most importantly, the qualitative picture of the electronic transitions is not affected severely, in comparison to what more accurate DFT or ab initio methods would predict, because the latter would only affect the tails of the wave functions and their energies, rather than the overlaps of the closely spaced orbitals. Thus, for the intramolecular energy relaxation and short-range intermolecular charge transfer processes, the nonadiabatic transitions rates are adequately described by the generalized gradient approximations (GGA), such as the PBE functional.

In our studies of the nonadiabatic dynamics in solid C_{60} we are interested in relaxation of the first (electron–hole recombination) and second (intraband relaxation) electronic excited states. Experimental studies indicate that the lowest energy singlet excited state of the C_{60} corresponds to the HOMO–LUMO transition.^{98,108} Density of states (DOS) presented in Figure 6a clearly shows that both HOMO and LUMO bands are formed by small sets of KS orbitals with close energy. Thus, the first excited state, denoted by EX1 in further discussions, can be represented by a mix of Slater determinants in which an electron is promoted from one of the KS orbitals of the HOMO band to one of the KS orbitals of the LUMO band. The average transition rate between

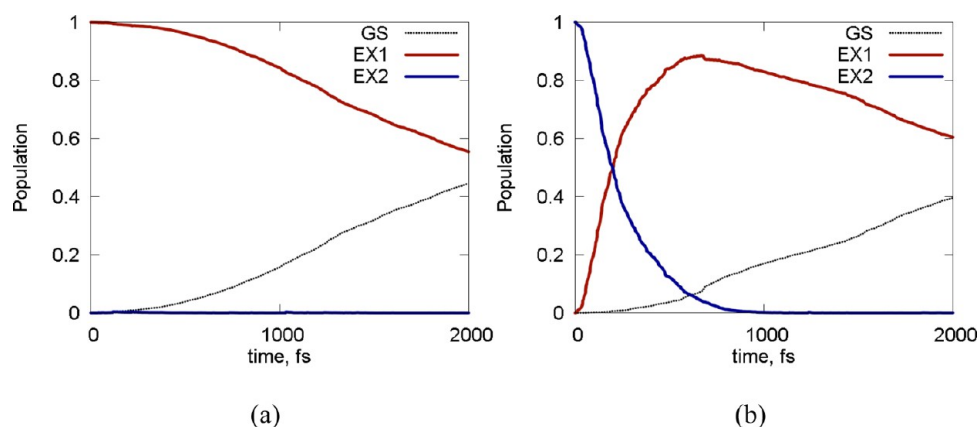


Figure 7. Relaxation dynamics in C_{60} without decoherence described by the FSSH scheme: (a) starting in the first excited state; (b) starting in the second excited state.

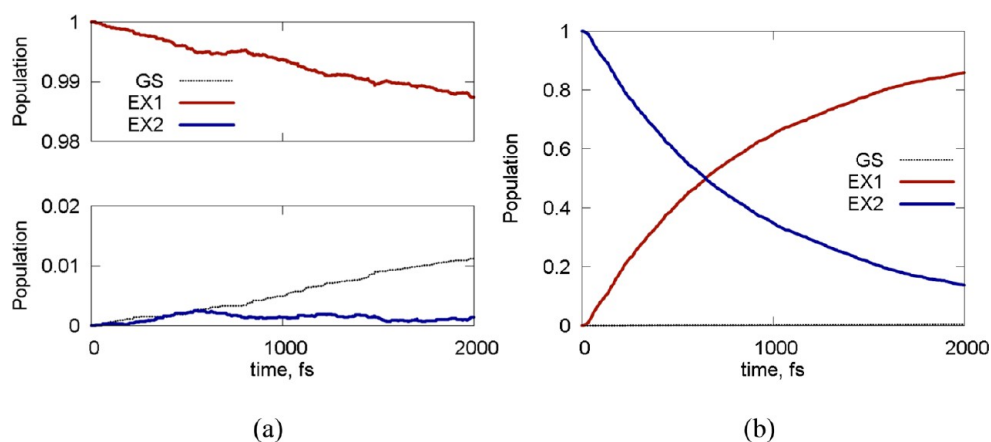


Figure 8. Relaxation dynamics in C_{60} with decoherence described by the DISH scheme: (a) starting in the first excited state; (b) starting in the second excited state.

the two groups of orbitals corresponds to the experimentally measured relaxation rate of the first excited state. For simplicity of analysis, we consider only the highest energy KS orbitals of the HOMO band and all KS orbitals of the LUMO (red arrow, EX1) band.

In this work, we also study the relaxation dynamics of the second excited state of solid C_{60} . This excited state is described similarly to the EX1, except we consider all KS orbitals of the LUMO+1 band (denoted by EX2, blue arrow) instead of the LUMO band. With such a description of the first two excited states of the C_{60} and with our “scissor operator” correction of the KS energy levels, the energy of the configurations from the first group (first excited state, EX1) is computed to be in the 1.6 to 2.0 eV range. The energy of the configurations from the second group (second excited state, EX2) lies in the 2.3–2.8 eV range; both are in agreement with experimental data.^{98,108} A typical time evolution of the lowest-energy configurations that belong to the EX1 and EX2 groups is shown in Figure 6b.

For each initial excitation level, we consider 10 initial molecular geometries, and for each of them, we compute 250 independent realizations of the stochastic FSSH and DISH processes. Therefore, the total number of evolutions is 2500, which provides good convergence of the statistical quantities computed. Each electronic evolution is integrated for 2 ps with the time step of 1 fs using the Liouville-based integrator described in section 2.1.

The relaxation dynamics computed with the fully coherent FSSH scheme for each of the two initial excitations considered is presented in Figure 7. The depopulation times obtained from the fit to the exponential part of the relaxation kinetics are 4.5 ps and 225 fs for the first excited (EX1, Figure 7a) and second excited (EX2, Figure 7b) states, respectively. These relaxation rates are significantly overestimated, by a factor of 5–20, compared to the experimental values.^{108,123}

We also compute the relaxation dynamics starting with the same initial excited states, while incorporating the decoherence effects via the DISH scheme, as explained in section 2.2. The results are presented in Figure 8. One can see that decoherence slows down the relaxation processes significantly. In particular, single exponential fits of the starting excited state population give the time scales of 148 ps and 970 fs for the first and second excited states, respectively. These time scales agree much better with the experimentally obtained results. Namely, the lowest energy exciton annihilation (LUMO to HOMO transition) in solid C_{60} completes on the time scale of >100 ps.¹⁰⁸ The intraband relaxation (LUMO+1 to LUMO) in water-dispersed C_{60} nanoparticles proceeds on the 1 ps time scale.¹²³ Our calculations are in excellent agreement with both experimental results.

To summarize this section, we have shown that decoherence may play a very important role in charge and energy transfer kinetics. Most of the time, it will slow down the processes by

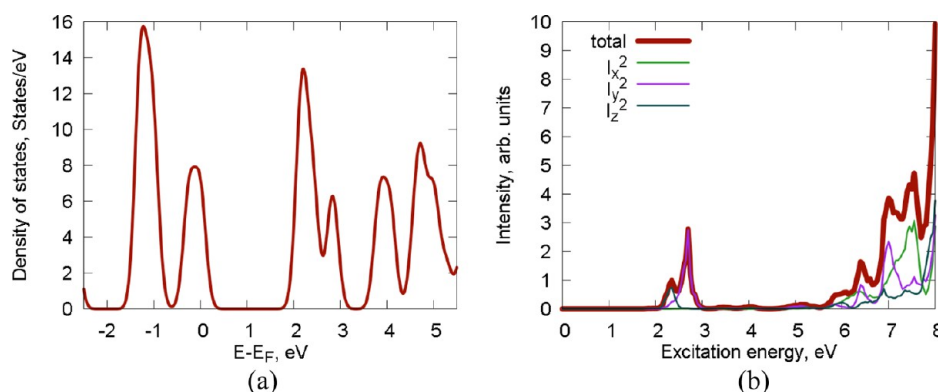


Figure 9. (a) DOS of the Si_6 cluster; (b) corresponding absorption spectrum.

several orders of magnitude. Considering this effect allows us to reproduce the experimentally measured relaxation time scales.

3.3. Multiexcitonic Basis States and Field–Matter Interaction. In the discussions presented above, as well as in our earlier work,⁵⁴ we have been dealing with excited states formed by promotion of an electron or a hole. At the same time, the basis states were not single KS orbitals, but rather Slater determinants constructed from them. Such a construction is very appealing, because it is very common in *ab initio* theories and is very flexible, allowing for more than one electron to be promoted from occupied to virtual KS levels. The latter capability is referred to here as the use of multiexcitonic states. A multiexcitonic state is understood as a Slater determinant with more than one excited electron (or hole). The use of multiexcitonic configurations can be inevitable in studies of processes that involve doubly and highly excited configurations as intermediates in electronic dynamics. Singlet fission and charge transfer dynamics in organic photovoltaic materials constitute notable examples.^{21–23} In this respect, such an approach will resemble that previously used by other authors.¹²⁴ Correlated dynamics of electrons and holes presents another important application of multiexcitonic states. For instance, electrons and holes can exchange energy by an Auger-type process.¹²⁵ Although only one electron is excited in this case, it may be crucial to consider all possible intermediate states, some of which may be not directly connected with each other by single particle transitions.

To illustrate the capabilities of the PYXAID program related to the use of multiexcitonic configurations and to the explicit treatment of the field–matter interaction at the photoexcitation stage, we apply the program to study multiexciton generation (MEG) in a small silicon cluster. MEG has been observed experimentally in a variety of materials, especially in semiconductor quantum dots.^{28,126,127} Among the most established mechanisms of exciton multiplication is the so-called impact ionization—the process inverse to the Auger recombination. We consider the Si_6 cluster, containing a magic number of atoms. Experimental¹²⁸ and previous theoretical^{82–84} studies of the MEG in Si quantum dots provide an excellent basis for verifying the validity of our calculations.

The DOS (Figure 9a) and the absorption spectrum (Figure 9b) of the Si_6 cluster are computed with the PYXAID code using output of the QE package, as described in detail earlier.⁵⁴ The computed DFT band gap of ca. 2.2 eV is in good agreement with the values reported previously.^{82,84,129} It is slightly larger than that of bigger size QDs, because the quantum confinement effects become stronger for smaller systems. The optical gap is in the same 2.2–2.5 eV range, corresponding to the ordinary

HOMO → LUMO excitation scheme. The HOMO–LUMO excitation leads to the standard one-electron-per-one-photon generation scheme and does not result in charge carrier multiplication. For the latter to occur, a photon with energy at least twice that of the band gap should be absorbed.²⁸ From the electronic absorption spectrum (Figure 9b), one can observe that the oscillator strength is very large starting at photon energies of ca. 6.0 eV, corresponding to more than two band gaps. Yet, there are weak transitions that can be induced by photons with smaller energies.

The nature of the MEG process dictates the choice of the basis states, which must include both singly (SE) and doubly (DE) excited configurations. The number of possible single configurations grows as $N_{\text{occ}} \times N_{\text{virt}}$, where N_{occ} and N_{virt} are the numbers of the occupied and virtual orbitals included in the active space, respectively. The number of doubly excited configurations grows even faster, as $(N_{\text{occ}} \times N_{\text{virt}})^2$. Thus, even relatively small numbers for N_{occ} and N_{virt} lead to enormous computational costs.

In particular, for the Si_6 cluster we compute 50 bands, 12 of which are occupied. The number of SE configurations is 456, while the number of DE configurations is ca. 208 000 (Figure 10a). As was discussed in section 2.1, integration scheme 0 shows encouraging computational efficiency and stability and can be applied to such large basis sets. However, because of the memory limitations, we limit our studies to no more than ~1000 states, which is still beyond the number of configurations typically needed in most of the applications. For this reason, we constructed a minimalistic model with the SE and DE

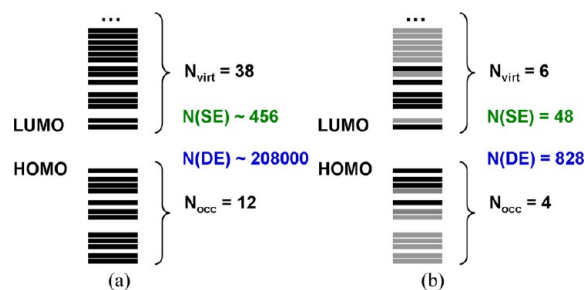


Figure 10. Construction of the basis set for the MEG simulation in the Si_6 cluster. (a) Scenario in which all possible single (SE) and double (DE) excitations from the $N_{\text{occ}} = 12$ occupied to the $N_{\text{virt}} = 38$ virtual orbitals are considered; (b) a minimalistic model in which the active space is composed of $N_{\text{occ}} = 4$ occupied and $N_{\text{virt}} = 6$ virtual orbitals, chosen randomly among the VB and CB orbitals, respectively. Gray lines denote the KS orbitals not included in the MEG modeling active space.

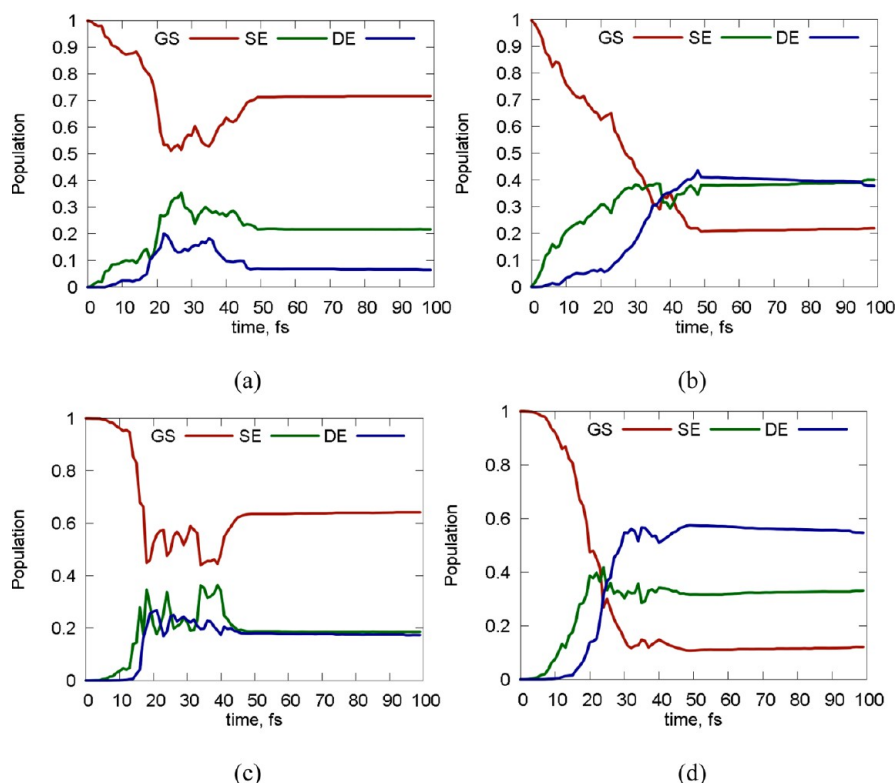


Figure 11. Dynamics of the photoexcitation and MEG in the Si_6 cluster for different photon energies and light pulse protocols: (a) $E = 2$ eV, protocol = 1; (b) $E = 4$ eV, protocol = 1; (c) $E = 2$ eV, protocol = 2; (d) $E = 4$ eV, protocol = 2. Fluence = $10 \text{ mJ}/\text{cm}^2$, $T = 50 \text{ fs}$, $dt = 0.1 \text{ fs}$, $N_{\text{occ}} = 4$, $N_{\text{virt}} = 5$. Excitation protocols 1 and 2 are defined in Figure 2.

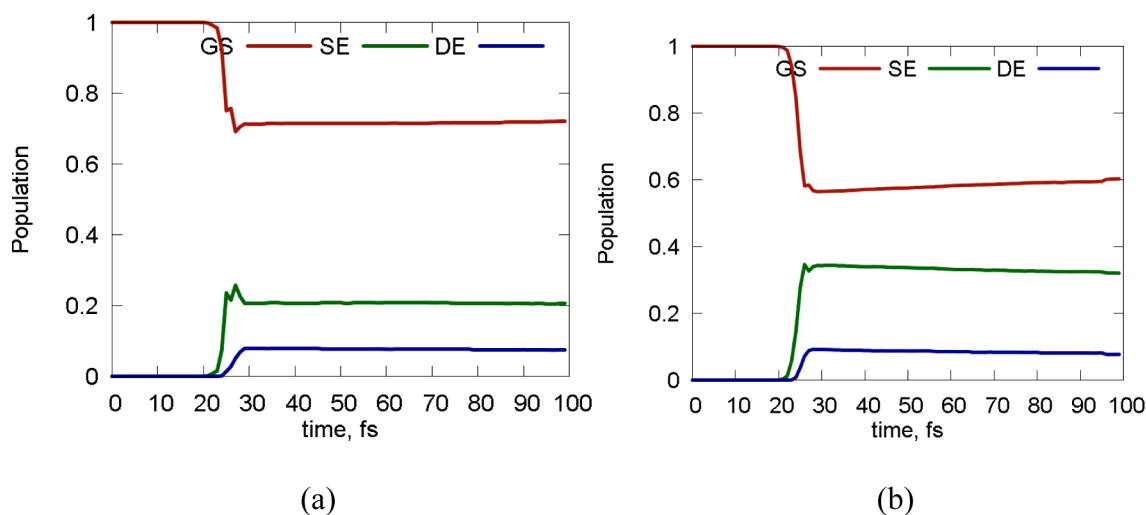


Figure 12. Dynamics of the photoexcitation and MEG in the Si_6 cluster for different photon energies: (a) $E = 2$ eV; (b) $E = 4$ eV. Fluence = $10 \text{ mJ}/\text{cm}^2$, modulation protocol = 2 (Figure 2), $T = 10 \text{ fs}$, $dt = 0.1 \text{ fs}$, $N_{\text{occ}} = 4$, $N_{\text{virt}} = 5$.

configurations formed of some evenly chosen KS orbitals spanning a wide range of excitation energies, as shown in Figure 10b. Such an approach demonstrates that the active space need not be constructed of a continuous set of the KS orbitals, but can consist of a small, finite set of orbitals. The corresponding procedures are implemented in the *lazy* module.

The results of simulations of the photoexcitation and MEG in the Si_6 cluster are presented in Figures 11–13. In all cases, the system starts in its ground electronic state. The interaction with the field initially creates SE configurations that may further be excited to yield DE states. We want to emphasize that DE

configurations can be produced not only by impact ionization of SE configurations with high energy but also by a sequential absorption of two photons with lower energy. In fact, if the two sequential photons excite the same electron, the overall result is equivalent to excitation of the system to one of its optically dark states. A similar effect is known to occur in a range of materials, such as fullerene, and is known as the photoinduced absorption.^{98,108,109} Therefore, the results of the modeling presented below are best understood in terms of simultaneously occurring MEG, multiple photon absorption, and relaxation processes.

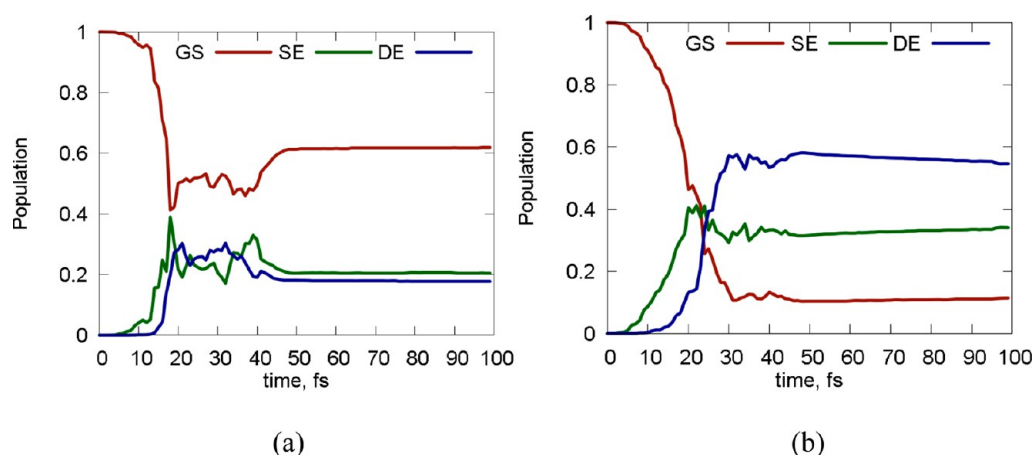


Figure 13. Dynamics of the photoexcitation and MEG in the Si_6 cluster for different photon energies: (a) $E = 2$ eV; (b) $E = 4$ eV. Fluence = $10 \text{ mJ}/\text{cm}^2$, modulation protocol = 2 (Figure 2), $T = 50$ fs, $dt = 0.1$ fs, $N_{\text{occ}} = 4$, $N_{\text{virt}} = 6$.

MEG drastically depends on the energy of incident photons. Therefore, we consider excitation conditions with two different incident photon energies, 2 and 4 eV. For the photon energies below the band gap of ~ 2.0 eV, no photoexcitation is observed, as it is expected. For photons with an energy of 2 eV, the only way to produce DE states is by a subsequent absorption of two photons. This restriction leads to a relatively small amount of DE configurations produced (Figure 11, panels a and c). On the contrary, the 4 eV photons can generate SE configurations that are capable of transforming into DE states by impact ionization, in addition to participating in a sequential two-photon absorption. The existence of these mechanisms leads to a notable increase of DE configurations produced. In addition, the relative fraction of DE with respect to the total number of excited configurations produced increases (Figure 11, panels b and d).

Not only is the magnitude of the photon energy important. The field-related parameters may bring interesting effects pointing to possible ways of controlling and improving MEG. To understand such an effect, for each photon energy we compute the time evolution of populations of the SE and DE states as functions of various laser pulse parameters: duration of the pulse, choice of the envelope function, and the number of basis states used. Dependence on the radiation intensity (fluence) is straightforward, and therefore, it is not discussed here explicitly. For all conditions tested, we use the average value of fluence, $10 \text{ mJ}/\text{cm}^2$, typically encountered in time-resolved spectroscopy measurements.

The effect of the field modulation protocol—one of the two possibilities implemented so far (see section 2.3)—is illustrated in Figure 11. One can observe that the sawtooth protocol (panels c and d) results in a more efficient overall photoexcitation. In addition, the DE/SE ratio also increases. The effect may be explained by the presence of an additional gradient of the field amplitude due to the modulation protocol, which eventually works as the one-way gate, increasing the probability flux in one direction. The analogy can be drawn with the unidirectional motion in molecular systems that can be induced by a periodic driving of control parameters affecting system properties.^{130,131} However, one should keep in mind that the modulation itself may require additional energy input. Therefore, one must estimate such energy requirements in order to accurately judge which of the modulation protocols delivers the maximal total energy gain.

For the rest of the tests, we use the sawtooth modulation protocol (2). The next important parameter affecting the photoexcitation efficiency is the pulse duration. The role of this parameter can be deduced by comparing Figures 11 (panels c and d) and 12, in which the pulse durations of 50 and 10 fs are used, respectively. One can see that shorter pulses lead to lower excitation efficiency. A short time pulse means that the system needs to respond to the external perturbation more quickly, in order to maximize the amount of energy it can absorb. However, the internal dynamics of the system is restricted. It is not able to accumulate all energy it is given, which leads to large energy losses. One can also think about this process from the thermodynamic point of view. It is known that energy losses are minimized when the processes occur adiabatically in the thermodynamic sense, i.e., sufficiently slowly. This condition is not satisfied when the field is modulated with a short period pulse, while it is the case for longer pulses.

Finally, we increase the size of the basis used for the simulations by including an additional KS level in the active space (Figure 13). Such a minor change of the active space increases the number of SE states from 40 to 48 and the number of DE states from 580 to 828. Field-related parameters are chosen as in the case of simulations shown in Figure 11 (panels c and d). One can observe that there are practically no changes in the observed dynamics of the excited states, despite the fact that the number of basis states has increased by more than 200. The result indicates that our minimalistic model is sufficient to produce reasonable description of the photoexcitation, charge carrier multiplication, and related processes in the Si_6 cluster.

The size of the basis set alone is not the only factor affecting the quality of the computational model. In particular, if the KS levels included in the active space are too far apart from each other on the energy scale, the resulting multielectron configurations will span a large range of energies. Among such configurations, only a few will be in the energy range of photons (< 4 eV in our case). Such a poor model will then predict incredibly low photoexcitation efficiencies (or no photoexcitation at all), even at extreme field parameters.

To summarize the finding of this section, we have demonstrated how the field–matter interaction can be included in direct simulation of photoexcitation processes. This tool allows one to investigate the detailed mechanism of charge and energy transfer during the photoexcitation step, rather than assuming that the system of interest is initially prepared in a

specific excited state. In particular, we have studied the initial kinetics of single and double exciton generation. We show that the choice of the laser pulse envelope may strongly affect the photoexcitation efficiency and the ratio of generated single and double excitons. The pulse duration is also important for the quantum yields of the photoexcitations. In general, longer pulses facilitate better excitation efficiencies. The energy of the absorbed photons also affects the efficiency of exciton generation—the larger the energy, the higher the efficiency. This observation is in line with the experimental results and other theoretical predictions.

CONCLUSIONS

We have presented a detailed formulation of advanced computational techniques implemented in the PYXAID package. To verify their implementation and to benchmark their performance, we applied them to a number of interesting problems: the hot electron relaxation dynamics in crystalline pentacene, the non-Markovian electron–hole recombination dynamics in solid C₆₀, and the direct photoexcitation and MEG in a small Si cluster.

Qualitative and quantitative comparison of different integration schemes has been carried out, as applied to the hot electron relaxation dynamics in solid pentacene. We show that the integration scheme based on the Liouville operator splitting method provides stability and accuracy properties superior to the Euler-type schemes. It allows one to use notably larger integration time steps for the electronic dynamics. The Liouville splitting method is comparable to the analytical integration method in accuracy and stability, but it is far more advantageous in terms of computational efficiency, providing acceleration up to several orders of magnitude. We argue that the use of such an integrator is strongly advisable in a number of cases: (a) when the electronic structure calculations are done on-the-fly, (b) when non-Markovian stochastic surface hopping algorithms, such as DISH, are used, (c) when the number of adiabatic basis states is very large, and (d) in any combinations of the above cases.

The importance of decoherence effects for correct prediction of the intra- and interband relaxation processes has been demonstrated with the electronic dynamics in solid C₆₀. The time scales for the LUMO+1 → LUMO and LUMO → HOMO processes computed with the fully coherent description are 225 fs and 4.5 ps, respectively. There, values are significantly underestimated in comparison to the experimental time scales of 1 ps and >100 ps, respectively. By incorporating the decoherence effects implemented via the DISH scheme, we obtain the time scales of 970 fs and 148 ps for the LUMO+1 → LUMO and LUMO → HOMO transitions, respectively, in excellent agreement with the experimental data.

Finally, we have demonstrated how the initial excitation can be prepared in an arbitrary system by direct coupling of the electronic dynamics to an external electromagnetic field. By including both singly and doubly excited configurations in the excitonic basis of the Si₆ cluster, we have been able to model their generation by single or multiple photon absorption and impact ionization, as well as their decay by nonadiabatic transitions. We conclude that the photon energy, laser pulse duration, and envelope function are all important factors determining the photoexcitation efficiency. In particular, as the photon energy or pulse duration increase, the overall population of excited configurations produced increases. The ratio of the DE to SE states also increases. The use of the sawtooth field envelope function leads to higher photoexcitation yields, and therefore it is

a more efficient protocol than the simple step-function pulse protocol.

The number of possible applications of the advanced capabilities of the PYXAID program is far greater and diverse than those demonstrated in the current paper. We have discussed the most probable types of applications, in which the advanced capabilities may come into play and become particularly important for efficient and accurate computations. We hope that these features will help users to gain a comprehensive understanding of fundamental mechanisms of electronic dynamics in various materials and systems.

ASSOCIATED CONTENT

Supporting Information

The derivation of the action of the Liouville operators of two types for solving the TD-SE; derivation of the field-matter interaction Hamiltonian matrix elements; and details of the relationship between the radiation fluence, field amplitude, and other parameters. This material is available free of charge via the Internet at <http://pubs.acs.org>.

AUTHOR INFORMATION

Corresponding Author

*E-mail: oleg.prezhdo@rochester.edu.

Notes

The authors declare no competing financial interest.

ACKNOWLEDGMENTS

A.V.A. was funded by the Computational Materials and Chemical Sciences Network (CMCSN) project at Brookhaven National Laboratory under contract DE-AC02-98CH10886 with the U.S. Department of Energy and supported by its Division of Chemical Sciences, Geosciences & Biosciences, Office of Basic Energy Sciences. O.V.P. acknowledges financial support of the U.S. Department of Energy, grant DE-SC0006527.

REFERENCES

- (1) Juban, E. A.; Smeigh, A. L.; Monat, J. E.; McCusker, J. K. *Coord. Chem. Rev.* **2006**, *250*, 1783–1791.
- (2) Akimov, A. V.; Neukirch, A. J.; Prezhdo, O. V. *Chem. Rev.* **2013**, *113*, 4496.
- (3) Tiwari, V.; Peters, W. K.; Jonas, D. M. *Proc. Natl. Acad. Sci.* **2012**, *110*, 1203–1208.
- (4) Shim, S.; Rebentrost, P.; Valleau, S.; Aspuru-Guzik, A. *Biophys. J.* **2012**, *102*, 649–660.
- (5) Hossein-Nejad, H.; Olaya-Castro, A.; Scholes, G. D. *J. Chem. Phys.* **2012**, *136*, 024112.
- (6) Fujita, T.; Brookes, J. C.; Saikin, S. K.; Aspuru-Guzik, A. *J. Phys. Chem. Lett.* **2012**, *3*, 2357–2361.
- (7) Balevičius, V.; Gelzinis, A.; Abramavicius, D.; Mančal, T.; Valkunas, L. *Chem. Phys.* **2012**, *404*, 94–102.
- (8) Vreven, T.; Bernardi, F.; Garavelli, M.; Olivucci, M.; Robb, M. A.; Schlegel, H. B. *J. Am. Chem. Soc.* **1997**, *119*, 12687–12688.
- (9) Weingart, O.; Migani, A.; Olivucci, M.; Robb, M. A.; Buss, V.; Hunt, P. J. *Phys. Chem. A* **2004**, *108*, 4685–4693.
- (10) Strambi, A.; Durbejj, B.; Ferré, N.; Olivucci, M. *Proc. Natl. Acad. Sci. U. S. A.* **2010**, *107*, 21322–21326.
- (11) Cohen, B.; Hare, P. M.; Kohler, B. *J. Am. Chem. Soc.* **2003**, *125*, 13594–13601.
- (12) Pecourt, J.-M. L.; Peon, J.; Kohler, B. *J. Am. Chem. Soc.* **2001**, *123*, 10370–10378.
- (13) Kohler, B. *J. Phys. Chem. Lett.* **2010**, *1*, 2047–2053.
- (14) Martsinovich, N.; Troisi, A. *Energy Environ. Sci.* **2011**, *4*, 4473.
- (15) Martsinovich, N.; Troisi, A. *J. Phys. Chem. C* **2011**, *115*, 11781–11792.

- (16) Anderson, N. A.; Lian, T. *Annu. Rev. Phys. Chem.* **2005**, *56*, 491–519.
- (17) Labat, F.; Ciofini, I.; Hratchian, H. P.; Frisch, M.; Raghavachari, K.; Adamo, C. *J. Am. Chem. Soc.* **2009**, *131*, 14290–14298.
- (18) Labat, F.; Le Bahers, T.; Ciofini, I.; Adamo, C. *Acc. Chem. Res.* **2012**, *45*, 1268–1277.
- (19) Tisdale, W. A.; Williams, K. J.; Timp, B. A.; Norris, D. J.; Aydil, E. S.; Zhu, X.-Y. *Science* **2010**, *328*, 1543–1547.
- (20) Muntwiler, M.; Yang, Q.; Zhu, X.-Y. *J. Electron. Spectrosc. Relat. Phenom.* **2009**, *174*, 116–124.
- (21) Chan, W.-L.; Ligges, M.; Jailaubekov, A.; Kaake, L.; Miaja-Avila, L.; Zhu, X.-Y. *Science* **2011**, *334*, 1541–1545.
- (22) Zimmerman, P. M.; Zhang, Z.; Musgrave, C. B. *Nat. Chem.* **2010**, *2*, 648–652.
- (23) Zimmerman, P. M.; Bell, F.; Casanova, D.; Head-Gordon, M. *J. Am. Chem. Soc.* **2011**, *133*, 19944–19952.
- (24) Kilina, S. V.; Kilin, D. S.; Prezhdo, O. V. *ACS Nano* **2009**, *3*, 93–99.
- (25) Kilina, S. V.; Neukirch, A. J.; Habenicht, B. F.; Kilin, D. S.; Prezhdo, O. V. *Phys. Rev. Lett.* **2013**, *110*, 180404.
- (26) Beard, M. C. *J. Phys. Chem. Lett.* **2011**, *2*, 1282–1288.
- (27) Ji, M.; Park, S.; Connor, S. T.; Mokari, T.; Cui, Y.; Gaffney, K. J. *Nano Lett.* **2009**, *9*, 1217–1222.
- (28) Nozik, A. J.; Beard, M. C.; Luther, J. M.; Law, M.; Ellingson, R. J.; Johnson, J. C. *Chem. Rev.* **2010**, *110*, 6873–6890.
- (29) Shalom, M.; Buhbut, S.; Tirosh, S.; Zaban, A. *J. Phys. Chem. Lett.* **2012**, *3*, 2436–2441.
- (30) Maeda, K.; Teramura, K.; Lu, D.; Takata, T.; Saito, N.; Inoue, Y.; Domen, K. *Nature* **2006**, *440*, 295–295.
- (31) Inoue, Y. *Energy Environ. Sci.* **2009**, *2*, 364.
- (32) Akimov, A. V.; Muckerman, J. T.; Prezhdo, O. V. *J. Am. Chem. Soc.* **2013**, *135*, 8682.
- (33) Shen, X.; Small, Y. A.; Wang, J.; Allen, P. B.; Fernandez-Serra, M. V.; Hybertsen, M. S.; Muckerman, J. T. *J. Phys. Chem. C* **2010**, *114*, 13695–13704.
- (34) Woodhouse, M.; Parkinson, B. A. *Chem. Soc. Rev.* **2009**, *38*, 197.
- (35) He, J.; Parkinson, B. A. *ACS Comb. Sci.* **2011**, *13*, 399–404.
- (36) Zheng, S.; Geva, E.; Dunietz, B. D. *J. Chem. Theory Comput.* **2013**, *9*, 1125–1131.
- (37) Phillips, H.; Zheng, S.; Hyla, A.; Laine, R.; Goodson, T.; Geva, E.; Dunietz, B. D. *J. Phys. Chem. A* **2012**, *116*, 1137–1145.
- (38) Phillips, H.; Geva, E.; Dunietz, B. D. *J. Chem. Theory Comput.* **2012**, *8*, 2661–2668.
- (39) Zheng, S.; Phillips, H.; Geva, E.; Dunietz, B. D. *J. Am. Chem. Soc.* **2012**, *134*, 6944–6947.
- (40) Walter, M. G.; Warren, E. L.; McKone, J. R.; Boettcher, S. W.; Mi, Q.; Santori, E. A.; Lewis, N. S. *Chem. Rev.* **2010**, *110*, 6446–6473.
- (41) Rühle, S.; Shalom, M.; Zaban, A. *Chem. Phys. Chem.* **2010**, *11*, 2290–2304.
- (42) Hagfeldt, A.; Boschloo, G.; Sun, L.; Kloo, L.; Pettersson, H. *Chem. Rev.* **2010**, *110*, 6595–6663.
- (43) Barbatti, M.; Granucci, G.; Lischka, H.; Ruckebauer, M. Newton-X: a package for Newtonian dynamics close to the crossing seam. www.uvie.ac.at/newtonx.
- (44) Barbatti, M.; Granucci, G.; Persico, M.; Ruckebauer, M.; Vazdar, M.; Eckert-Maksić, M.; Lischka, H. *J. Photochem. Photobiol. Chem.* **2007**, *190*, 228–240.
- (45) Werner, H.-J.; Knowles, P. J.; Knizia, G.; Manby, F. R.; Schütz, M.; Celani, P.; Korona, T.; Lindh, R.; Mitrushenkov, A.; Rauhut, G.; Shamasundar, K. R.; Adler, T. B.; Amos, R. D.; Bernhardsson, A.; Berning, A.; Cooper, D. L.; Deegan, M. J. O.; Dobbyn, A. J.; Eckert, F.; Goll, E.; Hampel, C.; Hesselmann, A.; Hetzer, G.; Hrenar, T.; Jansen, G.; Köppl, C.; Liu, Y.; Lloyd, A. W.; Mata, R. A.; May, A. J.; McNicholas, S. J.; Meyer, W.; Mura, M. E.; Nicklass, A.; O'Neill, D. P.; Palmieri, P.; Peng, D.; Pflüger, K.; Pitzer, R.; Reiher, M.; Shiozaki, T.; Stoll, H.; Stone, A. J.; Tarroni, R.; Thorsteinsson, T.; Wang, M. *MOLPRO*, version 2012.1; Institut für Theoretische Chemie, Universität Stuttgart: Stuttgart, Germany, 2012.
- (46) Levine, B. G.; Coe, J. D.; Virshup, A. M.; Martínez, T. J. *Chem. Phys.* **2008**, *347*, 3–16.
- (47) Thiel, W. *MNDO program*; Max Planck Institute für Kohlenforschung: Mulheim an der Ruhr, 2007.
- (48) Fabiano, E.; Keal, T. W.; Thiel, W. *Chem. Phys.* **2008**, *349*, 334–347.
- (49) Doltsinis, N.; Marx, D. *Phys. Rev. Lett.* **2002**, *88*, 166402–1.
- (50) CPMD. <http://www.cpmid.org>.
- (51) Marques, M. A. L.; Castro, A.; Bertsch, G. F.; Rubio, A. *Comput. Phys. Commun.* **2003**, *151*, 60–78.
- (52) Castro, A.; Appel, H.; Oliveira, M.; Rozzi, C. A.; Andrade, X.; Lorenzen, F.; Marques, M. A. L.; Gross, E. K. U.; Rubio, A. *Phys. Status Solidi B* **2006**, *243*, 2465–2488.
- (53) Andrade, X.; Alberdi-Rodriguez, J.; Strubbe, D. A.; Oliveira, M. J. T.; Nogueira, F.; Castro, A.; Muguerza, J.; Arruabarrena, A.; Louie, S. G.; Aspuru-Guzik, A.; Rubio, A.; Marques, M. A. L. *J. Phys.: Condens. Matter* **2012**, *24*, 233202.
- (54) Akimov, A. V.; Prezhdo, O. V. *J. Chem. Theory Comput.* **2013**, *9* (11), 4959–4972.
- (55) Jaeger, H. M.; Fischer, S.; Prezhdo, O. V. *J. Chem. Phys.* **2012**, *137*, 22A545.
- (56) Tully, J. C. *J. Chem. Phys.* **1990**, *93*, 1061–1071.
- (57) Trotter, H. F. *Proc. Am. Math. Soc.* **1959**, *10*, 545–551.
- (58) Raedt, H. D.; Raedt, B. D. *Phys. Rev.* **1983**, *28*, 3575–3580.
- (59) Misra, B.; Sudarshan, E. C. G. *J. Math. Phys.* **1977**, *18*, 756.
- (60) Petrosky, T.; Tasaki, S.; Prigogine, I. *Phys. Lett.* **1990**, *151*, 109–113.
- (61) Itano, W. M.; Heinzen, D. J.; Bollinger, J. J.; Wineland, D. J. *Phys. Rev.* **1990**, *41*, 2295.
- (62) Petrosky, T.; Tasaki, S.; Prigogine, I. *Physica A* **1991**, *170*, 306–325.
- (63) Prezhdo, O. V. *Phys. Rev. Lett.* **2000**, *85*, 4413–4417.
- (64) Mukamel, S. *Principles of Nonlinear Optical Spectroscopy*; Oxford University Press: New York, 1995.
- (65) Prezhdo, O. V.; Rossky, P. J. *J. Chem. Phys.* **1997**, *107*, S863–S878.
- (66) Prezhdo, O. V.; Rossky, P. J. *Phys. Rev. Lett.* **1998**, *81*, S294–S297.
- (67) Hwang, H.; Rossky, P. J. *J. Chem. Phys.* **2004**, *120*, 11380.
- (68) Neria, E.; Nitzan, A. *J. Chem. Phys.* **1993**, *99*, 1109.
- (69) Bittner, E. R.; Rossky, P. J. *J. Chem. Phys.* **1995**, *103*, 8130.
- (70) Bedard-Hearn, M. J.; Larsen, R. E.; Schwartz, B. J. *J. Chem. Phys.* **2005**, *123*, 234106.
- (71) Larsen, R. E.; Bedard-Hearn, M. J.; Schwartz, B. J. *J. Phys. Chem. B* **2006**, *110*, 20055–20066.
- (72) Habenicht, B.; Craig, C.; Prezhdo, O. *Phys. Rev. Lett.* **2006**, *96*, 187401.
- (73) Habenicht, B.; Prezhdo, O. *Phys. Rev. Lett.* **2008**, *100*, 197402.
- (74) Prezhdo, O. V. *J. Chem. Phys.* **1999**, *111*, 8366.
- (75) Zhu, C.; Jasper, A. W.; Truhlar, D. G. *J. Chem. Phys.* **2004**, *120*, 5543.
- (76) Zhu, C.; Nangia, S.; Jasper, A. W.; Truhlar, D. G. *J. Chem. Phys.* **2004**, *121*, 7658.
- (77) Shen, N.; Subotnik, J. E.; Yang, W. *J. Chem. Phys.* **2011**, *135*, 024101.
- (78) Bittner, E. R.; Rossky, P. J. *J. Chem. Phys.* **1997**, *107*, 8611.
- (79) Prezhdo, O. V.; Rossky, P. J. *J. Chem. Phys.* **1997**, *107*, 825–834.
- (80) Wong, K. F.; Rossky, P. J. *J. Chem. Phys.* **2002**, *116*, 8429.
- (81) Granucci, G.; Persico, M.; Zocante, A. *J. Chem. Phys.* **2010**, *133*, 134111.
- (82) Madrid, A. B.; Hyeon-Deuk, K.; Habenicht, B. F.; Prezhdo, O. V. *ACS Nano* **2009**, *3*, 2487–2494.
- (83) Hyeon-Deuk, K.; Prezhdo, O. V. *Nano Lett.* **2011**, *11*, 1845–1850.
- (84) Hyeon-Deuk, K.; Prezhdo, O. V. *ACS Nano* **2012**, *6*, 1239–1250.
- (85) Duncan, W. R.; Stier, W. M.; Prezhdo, O. V. *J. Am. Chem. Soc.* **2005**, *127*, 7941–7951.
- (86) Stier, W.; Duncan, W. R.; Prezhdo, O. V. *Adv. Mater.* **2004**, *16*, 240–244.
- (87) Long, R.; English, N. J.; Prezhdo, O. V. *J. Am. Chem. Soc.* **2012**, *134*, 14238–14248.
- (88) Kilin, D. S.; Micha, D. A. *J. Phys. Chem. C* **2009**, *113*, 3530–3542.

- (89) Kilin, D. S.; Micha, D. A. *J. Phys. Chem. C* **2011**, *115*, 770–775.
- (90) Wang, L.; Ernstorfer, R.; Willig, F.; May, V. *J. Phys. Chem. B* **2005**, *109*, 9589–9595.
- (91) Wang, L.; Willig, F.; May, V. *J. Chem. Phys.* **2006**, *124*, 014712.
- (92) Wang, L.; Willig, F.; May, V. *J. Chem. Phys.* **2007**, *126*, 134110.
- (93) Abe, R.; Sayama, K.; Domen, K.; Arakawa, H. *Chem. Phys. Lett.* **2001**, *344*, 339–344.
- (94) Fu, N.; Jin, Z.; Wu, Y.; Lu, G.; Li, D. *J. Phys. Chem. C* **2011**, *115*, 8586–8593.
- (95) Sayama, K.; Mukasa, K.; Abe, R.; Abe, Y.; Arakawa, H. *J. Photochem. Photobiol. Chem.* **2002**, *148*, 71–77.
- (96) Yun, H. J.; Lee, H.; Kim, N. D.; Lee, D. M.; Yu, S.; Yi, J. *ACS Nano* **2011**, *5*, 4084–4090.
- (97) Kakaliotis, J.; Street, R. A.; Jackson, W. B. *Phys. Rev. Lett.* **1987**, *59*, 1037.
- (98) Cheville, R. A.; Halas, N. J. *Phys. Rev. B* **1992**, *45*, 4548.
- (99) Fleischer, S. B.; Ippen, E. P.; Dresselhaus, G.; Dresselhaus, M. S.; Rao, A. M.; Zhou, P.; Eklund, P. C. *Appl. Phys. Lett.* **1993**, *62*, 3241.
- (100) Strümpfer, J.; Şener, M.; Schulten, K. *J. Phys. Chem. Lett.* **2012**, *3*, 536–542.
- (101) Pachón, L. A.; Brumer, P. *J. Phys. Chem. Lett.* **2011**, *2*, 2728–2732.
- (102) Shenvi, N.; Roy, S.; Tully, J. C. *J. Chem. Phys.* **2009**, *130*, 174107.
- (103) Fischer, S. A.; Chapman, C. T.; Li, X. *J. Chem. Phys.* **2011**, *135*, 144102.
- (104) Weaver, J. H.; Martins, J. L.; Komeda, T.; Chen, Y.; Ohno, T. R.; Kroll, G. H.; Troullier, N.; Haufler, R. E.; Smalley, R. E. *Phys. Rev. Lett.* **1991**, *66*, 1741.
- (105) Jost, M. B.; Troullier, N.; Poirier, D. M.; Martins, J. L.; Weaver, J. H.; Chibante, L. P. F.; Smalley, R. E. *Phys. Rev. B* **1991**, *44*, 1966.
- (106) Martins, J. L.; Troullier, N.; Weaver, J. H. *Chem. Phys. Lett.* **1991**, *180*, 457–460.
- (107) Juhasz, T.; Hu, X. H.; Suarez, C.; Bron, W. E.; Maiken, E.; Taborek, P. *Phys. Rev. B* **1993**, *48*, 4929.
- (108) Dexheimer, S. L.; Vareka, W. A.; Mittleman, D.; Zettl, A.; Shank, C. V. *Chem. Phys. Lett.* **1995**, *235*, 552–557.
- (109) Brorson, S. D.; Kelly, M. K.; Wenschuh, U.; Buhleier, R.; Kuhl, J. *Phys. Rev. B* **1992**, *46*, 7329.
- (110) Gianozzi, P.; Baroni, S.; Bonini, N.; Calandra, M.; Car, R.; Cavazzoni, C.; Ceresoli, D.; Chiarotti, G. L.; Cococcioni, M.; Dabo, I.; Dal Corso, A.; de Gironcoli, S.; Fabris, S.; Fratesi, G.; Gebauer, R.; Gerstmann, U.; Gougoussis, C.; Kokalj, A.; Lazzeri, M.; Martin-Samos, L.; Marzari, N.; Mauri, F.; Mazzarello, R.; Paolini, S.; Pasquarello, A.; Paulatto, L.; Sbraccia, C.; Scandolo, S.; Sclauzero, G.; Seitsonen, A. P.; Smogunov, A.; Umari, P.; Wentzcovitch, R. M. *J. Phys.: Condens. Matter* **2009**, *21*, 395592.
- (111) Perdew, J. P.; Burke, K.; Ernzerhof, M. *Phys. Rev. Lett.* **1996**, *77*, 3865–3868.
- (112) Perdew, J. P.; Burke, K.; Ernzerhof, M. *Phys. Rev. Lett.* **1997**, *78*, 1396.
- (113) Vanderbilt, D. *Phys. Rev. B* **1990**, *41*, 7892.
- (114) Verlet, L. *Phys. Rev.* **1967**, *159*, 98–103.
- (115) Andersen, H. C. *J. Chem. Phys.* **1980**, *72*, 2384–2393.
- (116) Reber, C.; Yee, L.; McKiernan, J.; Zink, J. I.; Williams, R. S.; Tong, W. M.; Ohlberg, D. A.; Whetten, R. L.; Diederich, F. *J. Phys. Chem.* **1991**, *95*, 2127–2129.
- (117) Hebard, A. F.; Haddon, R. C.; Fleming, R. M.; Kortan, A. R. *Appl. Phys. Lett.* **1991**, *59*, 2109.
- (118) Shirley, E. L.; Benedict, L. X.; Louie, S. G. *Phys. Rev. B* **1996**, *54*, 10970.
- (119) Mi, Y.; Odaka, H.; Iwata, S. *Jpn. J. Appl. Phys.* **1999**, *38*, 3453–3458.
- (120) Johnson, K. A.; Ashcroft, N. W. *Phys. Rev. B* **1998**, *58*, 15548.
- (121) Godby, R. W.; Schlüter, M.; Sham, L. J. *Phys. Rev. B* **1988**, *37*, 10159.
- (122) Gygi, F.; Baldereschi, A. *Phys. Rev. Lett.* **1989**, *62*, 2160–2163.
- (123) Ishibashi, Y.; Arinishi, M.; Katayama, T.; Miyasaka, H.; Asahi, T. *Chem. Lett.* **2012**, *41*, 1104–1106.
- (124) Greyson, E. C.; Vura-Weis, J.; Michl, J.; Ratner, M. A. *J. Phys. Chem. B* **2010**, *114*, 14168–14177.
- (125) Efros, A. L.; Kharchenko, V. A.; Rosen, M. *Solid State Commun.* **1995**, *93*, 281–284.
- (126) Nozik, A. J. *Inorg. Chem.* **2005**, *44*, 6893–6899.
- (127) Nozik, A. J. *Chem. Phys. Lett.* **2008**, *457*, 3–11.
- (128) Beard, M. C.; Knutsen, K. P.; Yu, P.; Luther, J. M.; Song, Q.; Metzger, W. K.; Ellingson, R. J.; Nozik, A. J. *Nano Lett.* **2007**, *7*, 2506–2512.
- (129) Fischer, S. A.; Madrid, A. B.; Isborn, C. M.; Prezhdo, O. V. *J. Phys. Chem. Lett.* **2009**, *1*, 232–237.
- (130) Chernyak, V.; Sinitsyn, N. *Phys. Rev. Lett.* **2008**, *101*, 160601–1–4.
- (131) Akimov, A. V.; Sinitsyn, N. A. *J. Chem. Phys.* **2011**, *135*, 224104.